UNIVERSITY OF TURKISH AERONAUTICAL ASSOCIATION

INSTITUTE OF SCIENCES AND TECHNOLOGY

MESO-SCALE FINITE ELEMENT MODELING OF

MICROVASCULAR CHANNELS IN COMPOSITES

MASTER THESIS

Ahmed Ali Abdull Hussein AL-SHAWK

Mechanical and Aeronautical Engineering Department

Master Thesis Program

June 2017

UNIVERSITY OF TURKISH AERONAUTICAL ASSOCIATION

INSTITUTE OF SCIENCES AND TECHNOLOGY

MESO-SCALE FINITE ELEMENT MODELING OF

MICROVASCULAR CHANNELS IN COMPOSITES

MASTER THESIS

Ahmed Ali Abdull Hussein AL-SHAWK
Ref. No:

IN PARTIAL FULFILMENT OF THE REQUIREMENT FOR THE DEGREE OF MASTER OF SCIENCE IN MECHANICAL AND AERONAUTICAL ENGINEERING

Thesis Supervisor: Asst. Prof. Dr. Barış SABUNCUOĞLU

June 2017

Ahmed Ali Abdull Hussein Al-shawk, having student number 1406080018 and enrolled in the Master Program at the Institute of science and Technology at the University of Turkish Aeronautical Association, after meeting all the required conditions contained in the related regulations, has successfully accomplished, in front of the jury, the presentation of the thesis prepared with the title of: "MESO-SCALE FINITE ELEMENT MODELING OF MICROVASCULAR CHANNELS IN COMPOSITES"

Thesis Supervisor: Asst. Prof. Dr. Barış SABUNCUOĞLU

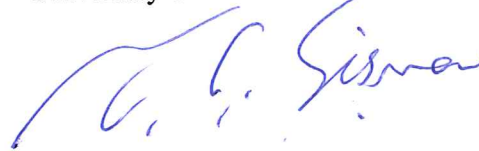University of Turkish Aeronautical Association

Jury Members: Assoc. Prof. Dr. Murat DEMİRAL

Çankaya University

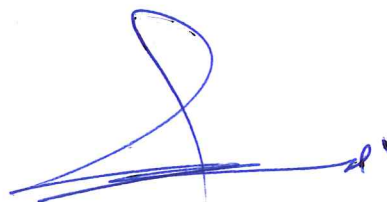Assoc. Prof. Dr. Tahsin Çağrı ŞİŞMAN

University of Turkish Aeronautical Association

Thesis Defense Date: 15. 06. 2017

ETHICAL DECLARATION

I hereby declare that all the information in this document has been obtained and presented in accordance with academic rules and ethical conduct. I also declare that, as required by these rules and conducts, I have fully cited and referenced all material and results that are not original to this work.

Ahmed A. AL-SHAWK

15/06/2017

ABSTRACT

MESO-SCALE FINITE ELEMENT MODELING OF

MICROVASCULAR CHANNELS IN COMPOSITES

Ahmed AL-SHAWK

Master Thesis, Department of Mechanical and Aeronautical Engineering

Supervisor: Assist. Prof. Dr. Barış SABUNCUOĞLU

June 2017, 72 pages

As the wide usage of composite materials in aerospace and automotive application, every new technological advancement must be investigated comprehensively. Because of its light weight and toughness, composites represent the best alternative for the heavy classical metals and alloys in the aerospace industry. The advancement of multifunctional composite structures empowered by embedded microvascular channels provides the potential for significant increases in functionality. Incorporating such microchannels leads to multifunctional composites by offering functions such as self-healing, active thermal and electromagnetic management. However, the presence of off-axis vascules leads to localized disturbance to the fibre architecture, i.e. resin-rich pockets, which are regarded as internal flaws and may cause stress concentrations within the composite structure.

The main aim of this study is to develop a computational modelling method and investigate the stress concentrations in composites with microvascular channels taking into consideration various vascular sizes, shapes and stacking sequences. The computational modelling for microvascular channels is accomplished by using a finite element approach. The model is generated using real dimension parameters of the tensile sample made in the UTAA labs by capturing these dimensions directly from the micro-pictures. The development of finite element model is performed in two stages. Initially, a model is generated as a 3D version of a previous plain strain model

and the results are compared for validation purposes. Then the developed 3D model is used to investigate the effect of microvascular channels on stresses for the samples prepared in UTAA. A more flexible model in boundary conditions, loading configurations, stacking sequence and channel direction is developed. The analysis results show that the stress above and through the middle of the resin-rich pocket preserve its behaviour for various vascular diameters with the same stacking order. Lowest normalized stresses are observed when the laminate above the pocket is in UD 0, while UD 90 normalized stresses are highest. Utilizing a microvascular channel as an elliptical shape rather than circular with the same cross-sectional area reduces the stress concentrations.

Keywords: Microvascular channels, FEM, composite, resin-rich pockets, fibre orientation.

ÖZET

KOMPOZİTLERDEKİ MİKROVASKÜLER KANALLARIN ORTA ÖLÇEKLİ SONLU ELEMAN MODELLEMESİ

Ahmed AL-SHAWK

Yüksek Lisans Tezi, Mekanik ve Havacılık Mühendisliği Bölümü

Tez Danışmanı, Yardımcı Doçent Doktor Barış SABUNCUOĞLU

2017, 72 sayfa

Kompozit malzemeler, havacılık ve otomotiv sanayisindeki uygulamalarda yaygın bir şekilde kullanım alanına sahip olduğundan, her yeni teknolojik ilerleme kapsamlı olarak araştırılmalıdır. Hafif ağırlığı ve sertliği sayesinde, kompozitler havacılık sanayisindeki ağır klasik metallere ve alaşımlara en iyi alternatif olmaktadır. Gömülü mikrovasküler kanallarla güçlendirilmiş olan çok fonksiyonlu kompozit yapıların ilerlemesi, işlevsellikte önemli artışlar için bir potansiyel sağlamaktadır. Bu tür mikro-kanalların dahil edilmesi, kendi kendine iyileşme, aktif termal ve elektromanyetik yönetim gibi fonksiyonlar sunarak, çok fonksiyonlu kompozitlerin elde edilmesine yol açmaktadır. Ancak, eksen dışı damarların varlığı, iç kusurlar olarak kabul edilen mesela reçine zengini cepler gibi lifli yapıya doğru lokalize bir bozulmaya neden olmaktadır ve kompozit yapı içerisinde gerilme yığışmalarına neden olabilir.

Bu çalışmanın ana amacı, sayısal bir modelleme yöntemi geliştirmek ve çeşitli damar boyları, şekilleri ve istif dizileri dikkate alınarak mikrovasküler kanallara sahip kompozitlerdeki gerilme yığışmasını araştırmaktır. Mikrovasküler kanallar için sayısal modelleme, bir sonlu eleman yaklaşımı kullanılarak elde edilmektedir. Model, THKÜ laboratuvarlarında yapılan germe numunesinin gerçek boyuttaki parametreleri kullanılarak, bu boyutların doğrudan mikro-resimlerle yakalanması vasıtasıyla üretilmektedir. Sonlu eleman modelinin geliştirilmesi iki aşamada gerçekleştirilmektedir. Başlangıçta, bir model daha önceki düzlemsel deformasyon

modelinin 3 boyutu olarak üretilmekte ve sonuçlar doğrulama amaçlı karşılaştırılmaktadır. Daha sonra geliştirilen 3 boyutlu model, THKÜ'da hazırlanan numuneler için mikrovasküler kanalların gerilmeler üzerindeki etkisini araştırmak için kullanılmaktadır. Sınır şartlarında daha esnek bir model, yükleme konfigürasyonları, istif dizisi ve kanal yönü geliştirilmiştir. Analiz sonuçları, reçine zengini cebin üzerindeki ve ortasındaki gerilmenin, aynı istif düzenine sahip çeşitli damar çapları için davranışını koruduğunu göstermektedir. Cebin üzerindeki lamine UD 0'da olduğunda en düşük normalleştirilmiş gerilmeler gözlenmişken UD 90'da normalleştirilmiş gerilmeler en yüksektir. Aynı kesite sahip olan daire şeklinden ziyade eliptik bir şekil olarak bir mikrovasküler kanalın kullanılması gerilme yığışımını düşürmektedir.

Anahtar sözcükler: Mikrovasküler kanallar, FEM, kompozit, reçine zengini cepler, lif oryantasyonu.

to my family...

ACKNOWLEDGMENT

CONTENTS

LIST OF TABLES

LIST OF FIGURES

LIST OF SYMBOLS AND ABBREVIATION

Symbols	Meaning
GFRP	Glass fibre reinforced polymer
UD	Uni-directional
FEM	Finite element method
FEA	Finite element analysis
HGT	Hollow glass tube
HGF	Hollow glass fibre
VaSC	Vaporisation of Sacrificial Components
PLA	Polylactic acid
SCF	Stress concentration factor

Abbreviations

E_i	Modulus of Elasticity on i direction, $i = 1, 2, 3$
v_{ij}	Poisson's ratio on ij planes, $i = 1, 2, 3$
G_{ij}	Shear Modulus on ij planes, $i = 1, 2, 3$
K	Bulk modulus
C_{ij}	Stiffness Matrix on ij planes, $i = 1, 2, 3$
θ	Fibre orientation angle
L_{RP}	Resin pocket length
h_d	Disturbance height
θ_d	Fibre disturbance angle
α	Thermal coefficient

CHAPTER ONE

INTRODUCTION

1.1   Aim and Objectives of the Study

The main aim of this study is to develop a computational modelling method and investigate the stress concentrations in composites with microvascular channels taking into consideration various vascule sizes, shapes and stacking sequences. The computational modelling for microvascular channels is accomplished by using a finite element approach. The model is generated using real dimension parameters of the tensile sample made in the UTAA labs by capturing these dimensions directly from the micro-pictures. The development of finite element model is performed in two stages. Initially, a model is generated as a 3D version of a previous plain strain model and the results are compared for validation purposes. Then the developed 3D model is used to investigate the effect of microvascular channels on stresses for the samples prepared in UTAA.

1.2   Research Methodology

The methodology used in this research is summarized schematically in Figure **1.1**. The study starts with the introduction to microvascular channels and brief description for the mechanics of composites. After those, the previous studies related to the microvascular channels in composites are presented. Then, the modelling procedures are introduced for the validation model and the present model. In this section, the parametric case studies with the present model are also introduced Then the results obtained by both models are presented and discussed. This section includes the results and the discussions of the case studies performed to understand the effect of vascule size and stacking orientation on the Mechanical behavior. Finally, the conclusions obtained from the entire study are presented and further recommendation are given.
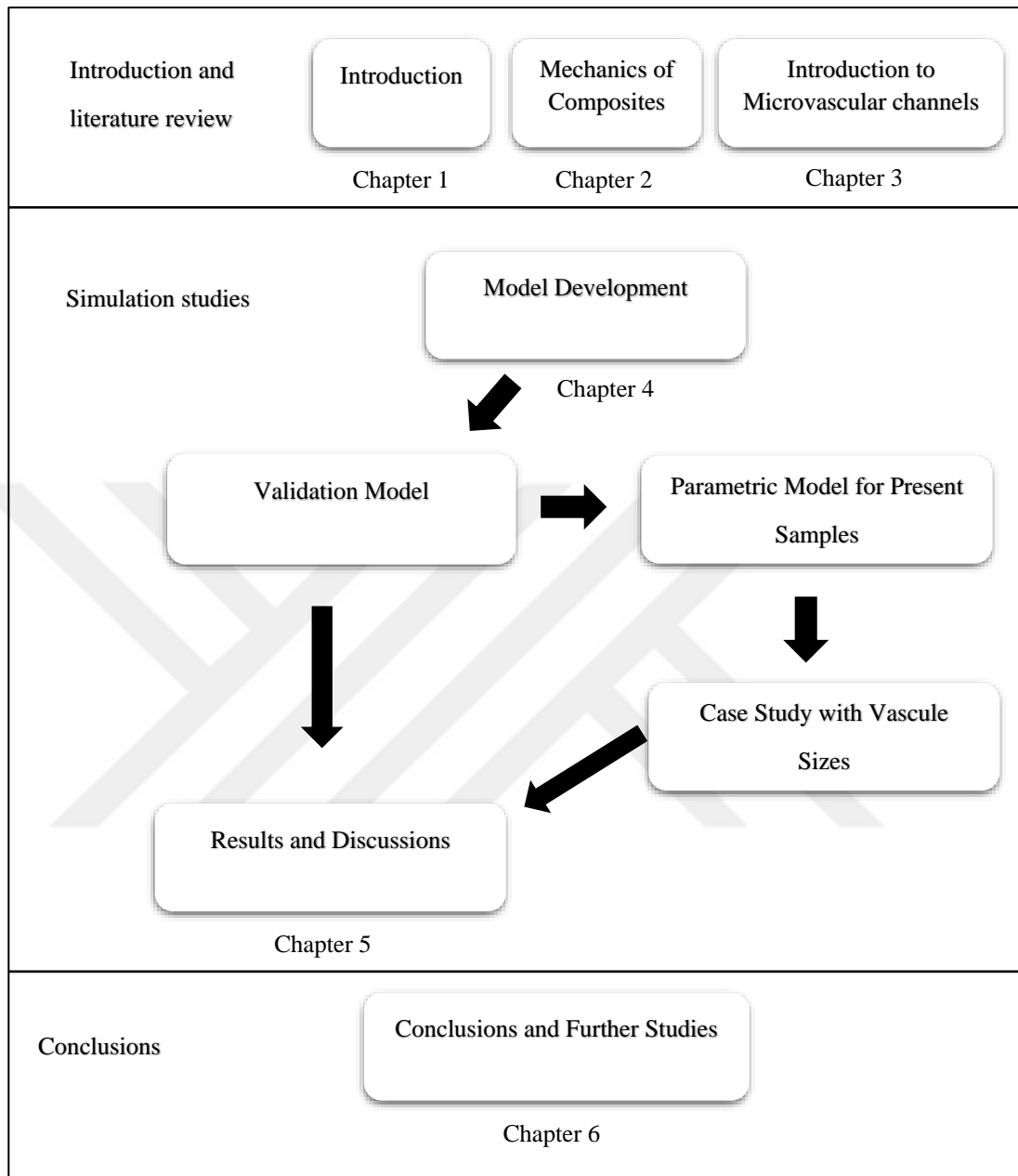
Figure 1.1: Research methodology of the study

1.3   Outline of the Study

The presented study consists of five chapters excluding this chapter. The summary of each chapter is given as follows:

Chapter Two, Mechanics of Composites: The mechanical behaviour theories of orthotropic material are introduced. Hooke's law for single lamina and composite laminate is briefly explained. Some principle concept related to the current study are presented.

Chapter Three, Microvascular Channels in Composites: The applications of the microvascular channels in composite are detailed. The manufacturing of microvascular channels and the mechanical assessment in the previous studies are reviewed. The manufacturing of the present sample in UTAA is also presented in this chapter. The chapter also includes the principles related to finite element method which is used in this study.

Chapter Four, Model Development: Modelling of composite laminate embedded with a microvascular channel is presented. The chapter includes, the modeling of verification model, present model and the case studies

Chapter Five, Results and Discussion: The results of the validation and present model are given. The results of parametric studies are discussed

Chapter Six, Conclusions: The summary and the outcomes of the performed research studies are presented. Some further studies are suggested based on this research.

CHAPTER TWO

MECHANICS OF COMPOSITES

2.1   Introduction to Composite Materials

It is hard to say undeniably when or where humans first learned about fibrous composites, nature provides us with numerous examples. Wood consists mainly of fibrous cellulose in a matrix of lignin, whereas most mammalian bone is made up of layered and oriented collagen fibrils in a protein-calcium phosphate matrix. The first examples of man-made fibrous composites are written in the book of Exodus in the old testament, and it was the straw-reinforced clay bricks used to build the 12 dynasty pyramids in Egypt. Also, the pottery found in northern Iraq and in central and south of America that contain plant fibres in it. These early uses of fibrous reinforcement probably resulted from the desire to prevent the cracks in the clay. Then the technological advancements led to inventing steel reinforced concrete in the twentieth century. More complicated composites are needed in the aviation and space equipment, in seeking for a new material that meets their demands [1].

In the 20th century, modern composites were used in the 1930s when glass fibres reinforced resins. Boats and aircraft were built out of these glass composites, commonly called *fibreglass*. Since the 1970s, application of composites has widely increased due to the development of new fibres such as carbon, boron, and aramids, and new composite systems with matrices made of metals and ceramics. To understand the mechanical characterization of a fibre reinforced composites, a brief background information for the basic concepts of composite macromechanical analysis are presented.

2.2   Macromechanical Analysis of Lamina

A thin layer of a composite material that is common of a thickness around 0.125mm is called lamina. Stacking of such laminae in the direction of lamina thickness constructs a laminate as illustrated in Figure **2.1**.
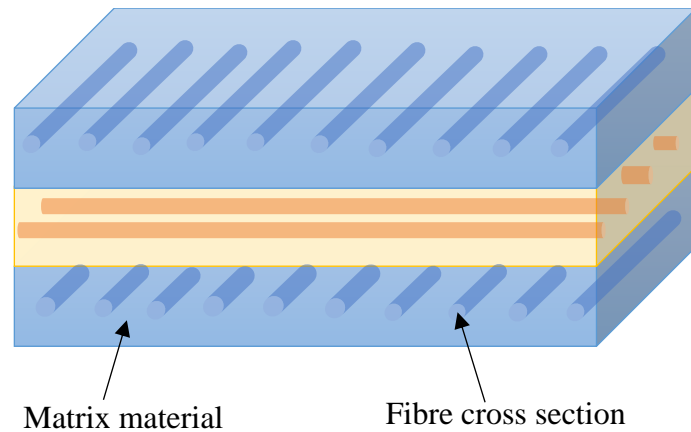
Figure 2.1: Typical laminate made of three laminas

Mechanical structures made of these laminates are subjected to various loads such as bending and twisting. The design and analysis of such laminated structures require knowledge of the stress and strain in the laminate. Also, failure assessment of the design demands the values of stress and strains parameters. The macromechanical analysis of a lamina is based on average properties and considering the lamina to be homogeneous. How to find these average properties is in the micromechanical analysis of the lamina, and it is beyond the area of this study. However, the mechanical behaviour for the homogenised lamina is still different than an isotropic material [2].

2.2.1 Hooke's Law for Isotropic - Orthotropic Materials

The materials whose properties like mechanical, physical, thermal and electrical is identical at each point and in any direction, are called isotropic material. Mechanically, there are only four different material constants which are the modulus of elasticity (E), Poisson's ratio (v), the shear modulus (G) and bulk modulus (K). Despite that fact, the isotropic materials have four different constants, two constants depend on the two other give the shear modulus and bulk modulus of elasticity as given in Equation 2.1 and Equation 2.2, respectively.

$$G = \frac{E}{2(1 + v)} \tag{2.1}$$

$$K = \frac{E}{3(1 - 2v)} \tag{2.2}$$

Although the isotropic material is the most widely used materials by engineers and designers, expanding knowledge about the anisotropic materials is a must due to the increasing use of composite material anisotropic materials in a wide range of applications. Anisotropic materials have different mechanical, physical, thermal and electrical properties at a point in different directions. The stress and the strain relationship using Hooke's Law can be written in indicial form as:

$$\sigma_i = \sum_{j=1}^{6} C_{ij}\varepsilon_j, \quad i = 1 \dots 6, \tag{2.3}$$

where (C_{ij}) is the stiffness matrix and has 36 constants as given in Equation (2.4) which is the general form of the stiffness matrix for anisotropic material.

$$\begin{bmatrix} \sigma_1 \\ \sigma_2 \\ \sigma_3 \\ \tau_{23} \\ \tau_{31} \\ \tau_{12} \end{bmatrix} = \begin{bmatrix} C_{11} & C_{12} & C_{13} & C_{14} & C_{15} & C_{16} \\ C_{21} & C_{22} & C_{23} & C_{24} & C_{25} & C_{26} \\ C_{31} & C_{32} & C_{33} & C_{34} & C_{35} & C_{36} \\ C_{41} & C_{42} & C_{43} & C_{44} & C_{45} & C_{46} \\ C_{51} & C_{52} & C_{53} & C_{54} & C_{55} & C_{56} \\ C_{61} & C_{62} & C_{63} & C_{64} & C_{65} & C_{66} \end{bmatrix} \begin{bmatrix} \varepsilon_{11} \\ \varepsilon_{22} \\ \varepsilon_{33} \\ \gamma_{23} \\ \gamma_{31} \\ \gamma_{12} \end{bmatrix} \tag{2.4}$$

From the strain energy considerations, it can be proved that elastic coefficient matrix is symmetric and the number of elastic coefficient matrix reduces to 21. Moreover, if the material system has three planes of material symmetry, such a material called as an orthotropic material. For an orthotropic material, there are 9 independent elastic constants and the stress-strain relationship has the form of Equation 2.5.

$$\begin{bmatrix} \sigma_1 \\ \sigma_2 \\ \sigma_3 \\ \tau_{23} \\ \tau_{31} \\ \tau_{12} \end{bmatrix} = \begin{bmatrix} C_{11} & C_{12} & C_{13} & 0 & 0 & 0 \\ C_{21} & C_{22} & C_{23} & 0 & 0 & 0 \\ C_{31} & C_{32} & C_{33} & 0 & 0 & 0 \\ 0 & 0 & 0 & C_{44} & 0 & 0 \\ 0 & 0 & 0 & 0 & C_{55} & 0 \\ 0 & 0 & 0 & 0 & 0 & C_{66} \end{bmatrix} \begin{bmatrix} \varepsilon_{11} \\ \varepsilon_{22} \\ \varepsilon_{33} \\ \gamma_{23} \\ \gamma_{31} \\ \gamma_{12} \end{bmatrix} \tag{2.5}$$

The 9 different elastic coefficients of an orthotropic material can also be formulated in terms of basic elastic constants as demonstrated in Equation. 2.6.

$$\begin{bmatrix} \sigma_1 \\ \sigma_2 \\ \sigma_3 \\ \tau_{23} \\ \tau_{31} \\ \tau_{12} \end{bmatrix} = \begin{bmatrix} \frac{1-v_{23}v_{32}}{E_2 E_3 \Delta} & \frac{v_{21}+v_{31}v_{23}}{E_2 E_3 \Delta} & \frac{v_{31}+v_{21}v_{32}}{E_2 E_3 \Delta} & 0 & 0 & 0 \\ \frac{v_{12}+v_{13}v_{32}}{E_3 E_1 \Delta} & \frac{1-v_{31}v_{13}}{E_3 E_1 \Delta} & \frac{v_{32}+v_{31}v_{12}}{E_3 E_1 \Delta} & 0 & 0 & 0 \\ \frac{v_{13}+v_{12}v_{23}}{E_1 E_2 \Delta} & \frac{v_{23}+v_{13}v_{21}}{E_1 E_2 \Delta} & \frac{1-v_{12}v_{21}}{E_1 E_2 \Delta} & 0 & 0 & 0 \\ 0 & 0 & 0 & 2G_{23} & 0 & 0 \\ 0 & 0 & 0 & 0 & 2G_{13} & 0 \\ 0 & 0 & 0 & 0 & 0 & 2G_{12} \end{bmatrix} \begin{bmatrix} \varepsilon_{11} \\ \varepsilon_{22} \\ \varepsilon_{33} \\ \gamma_{23} \\ \gamma_{31} \\ \gamma_{12} \end{bmatrix} \quad (2.6)$$

where,

$$\Delta = \frac{1 - v_{12}v_{21} - v_{23}v_{32} - v_{31}v_{13} - 2v_{12}v_{23}v_{31}}{E_1 E_2 E_3}$$

2.2.2 Hooke's Law for a Single Lamina

When the thickness of a single lamina is relatively small, out of plane loads can be neglected and Hooke's Law for orthotropic materials can be written for plane stress case

$$\begin{bmatrix} \sigma_1 \\ \sigma_2 \\ \tau_{12} \end{bmatrix} = \begin{bmatrix} Q_{11} & Q_{12} & 0 \\ Q_{12} & Q_{22} & 0 \\ 0 & 0 & Q_{66} \end{bmatrix} \begin{bmatrix} \varepsilon_1 \\ \varepsilon_2 \\ \gamma_{12} \end{bmatrix} \quad (2.7)$$

Where

$$Q_{11} = \frac{E_1}{1 - v_{21}v_{12}},$$
$$Q_{12} = \frac{v_{12}E_2}{1 - v_{21}v_{12}},$$
$$Q_{22} = \frac{E_2}{1 - v_{21}v_{12}}, \text{and}$$
$$Q_{66} = G_{12}.$$

If the ply is an angle ply such as given in Figure **2.2**. The stresses in a single lamina in the global coordinates can be found by multiplying with a rotation matrix

$$\begin{bmatrix} \sigma_x \\ \sigma_y \\ \tau_{xy} \end{bmatrix} = [T]^{-1} \begin{bmatrix} \sigma_1 \\ \sigma_2 \\ \tau_{12} \end{bmatrix}, \quad (2.8)$$

where [T] is called the transformation matrix and is defined as

$$[T]^{-1} = \begin{bmatrix} Cos^2\theta & Sin^2\theta & -2Sin\theta.Cos\theta \\ Sin^2\theta & Cos^2\theta & 2Sin\theta.Cos\theta \\ Sin\theta.Cos\theta & -Sin\theta.Cos\theta & Cos^2\theta - Sin^2\theta \end{bmatrix} \qquad (2.9)$$
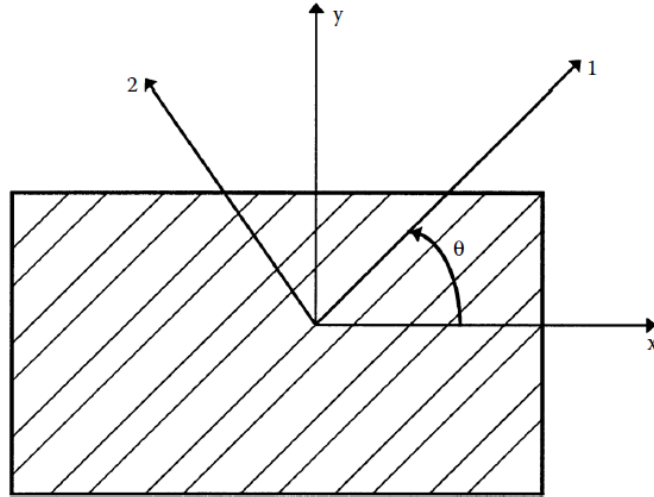
Figure 2.2: Local and global axis of an angle ply lamina [2]

2.3   Macromechanical Analysis of Laminate

In previous section stress–strain equations were developed for a single lamina. Yet, a real structure will not consist of a single lamina but a laminate consisting of multiple laminas bonded together through their thickness. Due to lamina thickness is very small in the order of (0.125mm), and the mechanical properties of a typical unidirectional lamina are severely limited in the transverse direction. If one stacks several unidirectional layers, this may be an optimum laminate for unidirectional loads. In the other hand, for complex loading and stiffness requirements, this would not be desirable. This problem can be overcome by stacking a laminate with layers at different angles for given loading and stiffness requirements. This approach increases the cost and weight of the laminate and thus it is necessary to improve the ply angles. Furthermore, layers of different composite material systems may be used to establish a more optimum laminate.

2.3.1 Stacking Sequence

A laminate is consisting of a number of laminas stacked in the thickness direction (z) as illustrated in Figure **2.3**. In uni-directional (UD) laminate, the same angle of fibre orientation (θ) is set for all laminas. If the orientation angle alternate between θ and $-\theta$ it is called angle-ply laminate. However, if θ alternate between 0 and 90 it is called a cross-ply laminate. The symmetric laminate consists of number of laminas that its orientation angles are symmetric about the midplane of the laminate as in the example below for $[0/\pm45/90]_s$:

0
45
-45
90
90
-45
45
0

It is also balanced because for every $+\theta$ there is a $-\theta$.
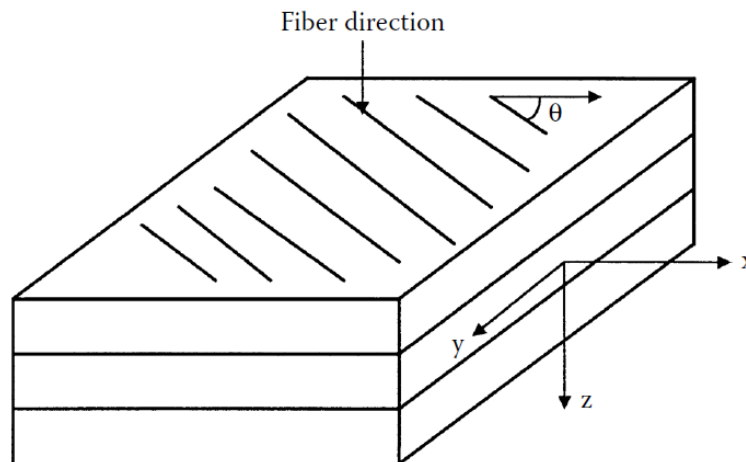
Figure 2.3: Schematic of a laminate [2]

2.3.2 Strain-Displacement Equations

The axial strain in a beam was related to the midplane strain and curvature of the beam under a uniaxial load and bending. In this section, similar relationships to that of a

lamina will be developed for a plate under in-plane loads such as shear and axial forces, and bending and twisting moments as displayed in Figure **2.4**. *The classical lamination theory* is used to develop these relationships. The following assumptions are made in the classical lamination theory to develop the relationships

- Each lamina is orthotropic, homogeneous, and behave in a linearly elastic manner.

- The laminate is thin and wide (width is much bigger than thickness).

- Strain distribution in the thickness direction is linear.

- Prefect interlaminar bond exists between the laminas.

The laminate strains are linearly related to distance from the midplane [3]. For the jth-lamina (Figure **2.4**) the strain equations can be written in a matrix form as follow:

$$\begin{Bmatrix} \varepsilon_{xx} \\ \varepsilon_{yy} \\ \gamma_{xy} \end{Bmatrix}^j = \begin{Bmatrix} \varepsilon_{xx}^\circ \\ \varepsilon_{yy}^\circ \\ \gamma_{xy}^\circ \end{Bmatrix} + z_j \begin{Bmatrix} k_{xx} \\ k_{yy} \\ k_{xy} \end{Bmatrix} \qquad (2.10)$$

Where,

$\varepsilon_{xx}^\circ, \varepsilon_{yy}^\circ$ are the midplane normal strains in the laminate, γ_{xy}° is the midplane shear strain in the laminate, k_{xx}, k_{yy} are the bending curvatures of the laminate, k_{xy} is the twisting curvature of the laminate, z_j is the Jth lamina distance from the midplane in the thickness direction.

Figure 2.4: Laminate geometry [3]

2.3.3 Laminate Forces and Moments

Applied force and moment resultant (Figure **2.5**) on a laminate are related to the midplane strains and curvatures by the subsequent equations:

$$\begin{Bmatrix} N_{xx} \\ N_{yy} \\ N_{xy} \end{Bmatrix} = [A] \begin{Bmatrix} \varepsilon_{xx}^{\circ} \\ \varepsilon_{yy}^{\circ} \\ \gamma_{xy}^{\circ} \end{Bmatrix} + [B] \begin{Bmatrix} k_{xx} \\ k_{yy} \\ k_{xy} \end{Bmatrix} \tag{2.11}$$

and

$$\begin{Bmatrix} M_{xx} \\ M_{yy} \\ M_{xy} \end{Bmatrix} = [B] \begin{Bmatrix} \varepsilon_{xx}^{\circ} \\ \varepsilon_{yy}^{\circ} \\ \gamma_{xy}^{\circ} \end{Bmatrix} + [D] \begin{Bmatrix} k_{xx} \\ k_{yy} \\ k_{xy} \end{Bmatrix} \tag{2.12}$$

where

N_{xx}, N_{yy} are the normal force per unit length, N_{xy} is the shear force per unit length, M_x, M_y are the bending moments per unit length, M_{xy} is the twisting moments per unit length.

The [A], [B], and [D] matrices are called the extensional (N/m), coupling (N), and bending (N.m) stiffness matrices, respectively.

11

Figure 2.5: Resultant forces and moments on a laminate [3]

2.3.4 Elements in the Stiffness Matrices

The elements in [A], [B], and [D] matrices are computed from

$$A_{mn} = \sum_{j=1}^{n} (\bar{Q}_{mn})_j (h_j - h_{j-1}) \tag{2.13}$$

$$B_{mn} = \frac{1}{2} \sum_{j=1}^{n} (\bar{Q}_{mn})_j (h_j^2 - h_{j-1}^2) \tag{2.14}$$

$$D_{mn} = \frac{1}{3} \sum_{j=1}^{n} (\bar{Q}_{mn})_j (h_j^3 - h_{j-1}^3) \tag{2.15}$$

where

(n) is the total number of laminas in the laminate, $(\bar{Q}_{mn})_j$ is the elements in the transformed stiffness matrix $[\bar{Q}]$ of the jth lamina, (h_{j-1}) is the distance from the midplane to the top of the jth lamina, (h_j) is the distance from the midplane to the bottom of the jth lamina.

After [A], [B], and [D] matrices, midplane stresses and strains and curvatures can be calculated by equations (2.11) and (2.12). The strains in each lamina can be found from (2.10) depending on their location. Then the stresses can be found by equations (2.7, 2.8).

CHAPTER THREE

MICROVASCULAR CHANNELS IN COMPOSITES

3.1   Introduction

As the wide usage of composite materials in aerospace and automotive application, every new technological advancement must be investigated comprehensively. Because of its light weight and toughness, composites represent the best alternative for the heavy classical metals and alloys in the aerospace industry. Over the last few decades, extensive efforts were made for composite materials in order to fulfil the future requirements [4, 5]. The latest Functionalizing techniques are done by incorporation of optical fibre [6, 7], piezoelectric materials & sensors [8, 9], nanoparticles especially CNTs [10-12] and shape memory polymers & alloys into the matrix directly during composite manufacturing [13-15]. However, these resultant composites had limitations in functionality due to their processing, this provides researchers with the opportunity to seek new beneficial ways. Biologically inspired microvascular systems, a new promising approach introduces the addition of microvascular channels inside the composite structure. numerous advantages obtained from the embodiment of the microvascular channels. From 1μm to 1mm diameter microvascular channels are introduced into polymers and polymer matrix composites with fluid filler to increase the functionality. Presently, these microvascular channels bringing additional functions such as active cooling [16, 17], self-healing [18-23], sensing [24, 25], enhanced damage visibility in composite structure [26, 27].

3.2   Microvascular Channels Manufacturing Methods

There are three main type of the microvascular channel manufacturing methods, the removable solid cores, non-removable hollow cores and direct ink writing.

3.2.1 Removable Solid Cores

The first method of microchannel creation by removable solid cores is very much the same procedure with the non-removable hollow cores method. First the positioning of the removable cores (metal or polymer) on the dry fabric layers. After that, resin permeation and curing in order to obtain a composite laminate. Finally, the removing of the cores to reveals the hollow channels as illustrated in Figure **3.1**.

The microchannel diameter by using polymer wires are (280μm-1.2mm) only straight and non-woven, while in metallic wires are (80-710μm) orthogonal hollow vascules. The advantages of this method are similar to the first method in excluding the surface-resin interface issues and reducing the effect on mechanical strength. On the other hand, the disadvantages are it is limited to straight channels, not suitable for thermal applications and produces an elliptical cross-section (only in polymer wires). The only application, for now, is self-healing [28-36].

3.2.2 Non-Removable Hollow Cores

The basic principle of non-removable hollow cores based on very simple techniques. An array of glass, metal, polymer tubes is placed in the middle of the fabric layers during composite production. At the time of curing, these embedded hollow tubes will serve as microchannels for different applications. The most common non-removable hollow cores method is:
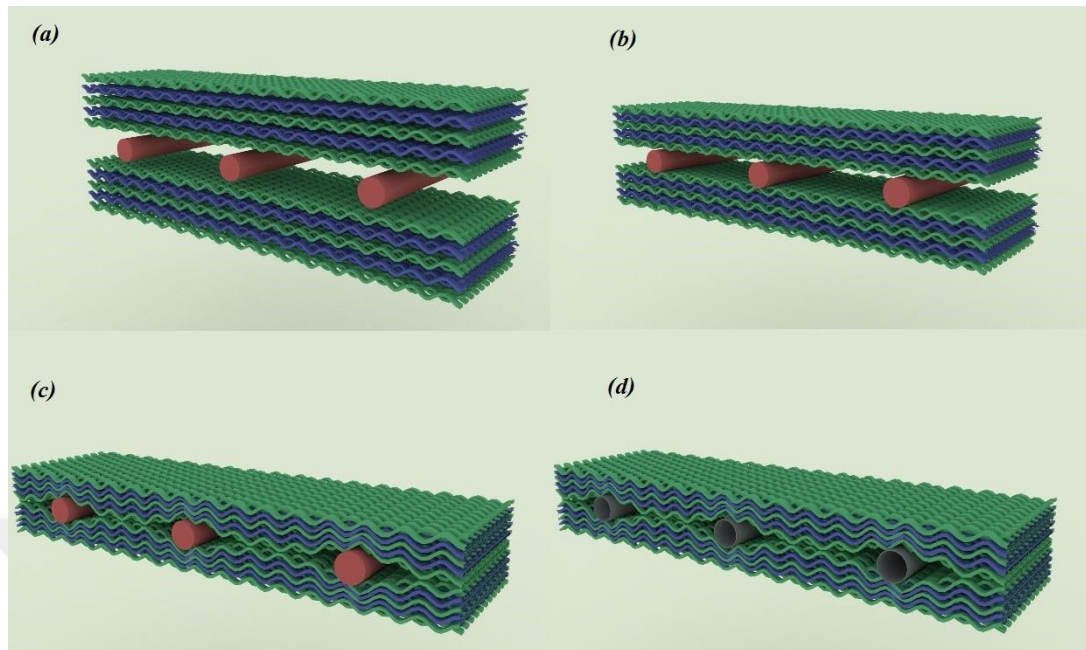
Figure 3.1: Graphical representation of microchannel creation by removable solid cores (a) positioning of solid cores (metallic or polymer) in the midst of dry fabric layers; (b) composite processing (hand lay-up, vacuum packaging, resin permeation, RTM or autoclave); (c) cured composite laminate; and (d) exposing the microchannels by manual removal of solid mandrels

3.2.2.1   Hollow Glass Tubes (HGT)

Many researchers used this type of microchannel [37-45]. A wide range of HGT diameters (0.3-3mm) with much smaller than the two methods above. The advantages of this method are easy positioning, compatible with most composite production techniques, even and very smooth internal surface, close controllability and much-compacted structure and higher structural strength. The main disadvantages of this method are the drop in mechanical properties when a large tube size is used, straight alignment only, size limitation >0.3mm only, not convenient with heat transfer and poor glass tube surface-resin interaction. HGT can be used in self-healing and self-sensing applications.

3.2.2.2   Hollow Glass Fibre (HGF)

This method of production microvascular channel composite introduces the smallest inner diameter of tubes, using HGF a hollow with a diameter of (5-60μm) was

produced. The main advantages of this method are developing a microvascular channel in woven laminate structure, so it has made many functional microvascular structures, much less impact on mechanical properties. HGS is compatible with most composite production techniques. Provides size and shape close controllability, a wide range of hollow tubes diameter can be embedded. The disadvantages of this method are the few limitations to size and type of microchannels, not convenient to heat transfer applications and efficient only with glass fibre reinforced composites. HGF microvascular channel composites used for self-healing and visual enhancement of internal damage applications [46-50].

3.2.3   Vaporisation of Sacrificial Components (VaSC)

This method technique encompasses the mechanised woven fabric containing a catalyst-saturated polylactic acid (PLA) sacrificial fibre stitched with glass or carbon fibres. Coordinated, 3D microchannels are produced by replacing a fibre tow with sacrificial fibres, and then a low viscosity resin infiltrates the structure. After curing, sacrificial fibres removed from the composite structure by vaporisation at 200°C followed by moderate vacuum, making a 3D microchannel network. The microchannel diameter ranging from 20 to 500µm. This method is compatible with parallel interconnected 3D and 3D woven. The advantages are, large variety in size, shape and microvascular structures, least impact on the mechanical properties, smooth internal surface, controllability over shape and size of the channel. While the disadvantages are, high-temperature resin requirement and require a skill for the formation and structuring the subsequent microvascular channels. This type of microchannels manufactured by VaSC can be used in thermal management, electrical conductivity tuning, electromagnetic signature and chemical reactivity applications [51-54].

There are other common manufacturing methods like non-removable metal tubes [37, 39], non-removable hollow polymer tubes [55], micromachining [36, 56-58], electrical discharge [59], Direct ink writing [15, 60-63].

3.2.4 Fabrication and Properties of the Present Specimen Samples

In the present study, the microvascular channels are generated via VaSC method. The tensile test samples are prepared using uni-directional glass fibre reinforced composite laminate specimens containing vascular channel (1mm diameter) along the laminate mid-plane. The laminate thickness is 4.5mm and consists of 16 plies uni-directional glass fabrics (areal weight of 330 g/m^2). The stacking orders for the laminate are ($[0/90]_{4s}$ and $[90/0]_{4s}$). Fabrics are cut and laid in an Aluminium mold (250 mm $\times$ 200 mm and thickness of 3 mm) according to the desired stacking order. Four PLA filaments with a diameter of 1 mm and 260 mm length are located in the mid-plane which is on the 8th ply with 30 mm apart from each other (Figure **3.2**). An empty space is kept for a specimen without a vascule for comparing the results. The PLA filaments are adhered from both ends to the mold surface in order to keep the filaments straight. The fibre volume fraction is 55%. Finally, the mould is bolted and fabrics are impregnated with epoxy resin (Aradur 564: Araldite 2954, 100:37 wt%, Huntsman) using Vacuum. The produced Composite are cured in an oven for one hour at 80°C then 4 hours at 160°C. The composite plates are trimmed from the edges and cut parallel to PLA filaments into an individual tensile test specimens (250 mm $\times$ 25 mm) after the curing process. Samples are put in a vacuum oven at 200°C for 24 hours to vaporise the PLA filaments (sacrificial component).
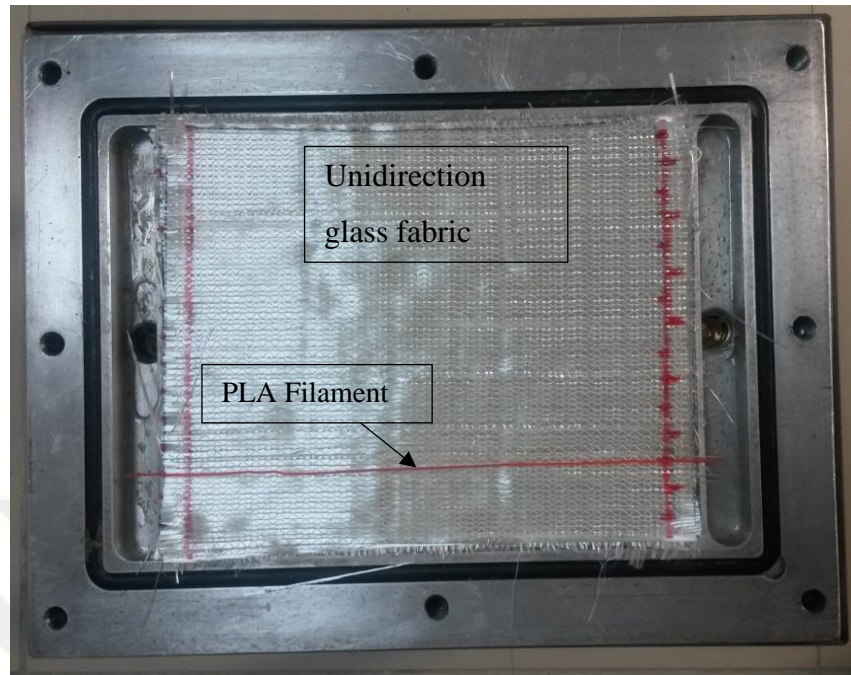
Figure 3.2: Mold arrangement

3.3 Mechanical Behaviour Assessment

Microvascular channels act as voids and stress concentration points and affect the mechanical strength of the composite laminate. The insertion of polymer\metallic wires and HGTs to the composite structure generates resin-rich pockets, increases the volume fracture and ply undulation. The researchers investigated and reported these effects on mechanical properties using both experimental tests and theoretical analysis, and determined the effect of the presence of microvascular channels on the tensile modulus, tensile strength, compression modulus, compression strength, interlaminar shear stress, flexural strength, compression after impact and fatigue strength of the composite structure [64]. However, an increase in the mode-I and mode-II fracture toughness was observed [38]. The mechanical test shows a realistic behaviour of the subject but the test trials are limited due to cost and effort. The most common experimental tests are a tensile test [5-7, 9, 39, 64, 65], compression test [6, 7, 33], drop-weight as a low energy impact test [6, 9, 39], Fatigue test [6, 9], short beam shear test and the double cantilever beam (DCB) test [65]. Cappola et al. [65]

18

studied the effect of a microchannel that produced in straight and woven-shaped networks glass fibre reinforced composite using VaSC on the tensile properties and damage evolution. They found negligible and modest (<10% reduction) effect of microchannels on the in-plain tensile and transverse moduli, by applying a tensile load on the microchannel structure in both transverse and longitudinal directions. Kousourakis et al. [64] reported that carbon reinforced composites that contain microchannel of 0.4-1.8mm diameters by the silicon mandrel and 0.17-0.68mm diameters by the HGT gave a similar dependence on the channel shape, size and orientation in both tensile and compressive strengths. They also found that these strengths of CFRP composite decreases slowly (<10% by the largest channel diameter) for longitudinal microchannels and rapidly (>50% by the largest channel diameter) for transverse microchannels. Huang et al. [33] examined the effect of microchannels (80-710μm diameter) implanted within CFRP composites, in the transverse direction, on the compression strength of CFRP composites. Their results showed a reduction in the compression strength of microchanneled CFRP composites from 13% to 70% depending on the channel diameter. They also noted that the most contribution in this reduction of compression strength resulted from fibre waviness and resin-rich regions. Patrick et al. [66] produced 3D microvascular networks both isolated (parallel) and interpenetrating (herringbone) using VaSC, these networks meant to carry healing fluids for self-healing of delamination damage, tested by DCB node-I fracture toughness test. The herringbone structure showed astonishing recovery (>100%) than parallel structure even after each cycle. The main tool that used to imitate these tests in order to fully assess them considering various aspects is finite element modelling programs, and that what will be discussed in next section.

3.4 Finite Element Modelling Method

3.4.1 Introduction

Many physical phenomena in engineering and science can be described in terms of partial differential equations. Even though, solving these equations by classical analytical methods for arbitrary shapes is almost impossible. The finite element method (FEM) is a numerical approach by which these partial differential equations

can be solved approximately. From an engineering standpoint, the FEM is a method for solving engineering problems such as stress analysis, heat transfer, fluid flow and electromagnetics by computer simulation [66]. The main idea of the FEM is to obtain an approximate solution by dividing the object into finite elements, connected by nodes.

In this thesis, the finite element method (FEM) is used as a tool to analyse the effect of different microchannel configurations by means of commercial solving software (ABAQUS/Standard) [67]. For effective use of any finite element solving software, understanding the fundamentals in the finite element is necessary, and because of FEM is a very broad subject. Therefore, in this section, the basic principle of FEM in solid mechanics is introduced. Finite element modelling represents the best choice to fully analyse the subjects after the validation with the experimental test results. And because of experiments requirements such as time, the required environment, effort and money. Finite element analysis (FEA) is chosen as an analysis method in this thesis. Different design parameter can be changed and tested theoretically with taking into consideration only the configurations of the specimens made by.

3.4.2 Basic FEM Procedure

The axial deformation of a rod is taken as a simple problem to clarify the theory. The ordinary differential equation (ODE) describing the deformation (u) of the rod is

$$-\frac{d}{dx}\left(EA\frac{du}{dx}\right) - f = 0 \quad ; \quad 0 \leq x \leq L \tag{3.1}$$

Where *E, A* are the modulus and cross-section area of the rod, respectively, and *f* is the distributed force. For the case illustrated in Figure **3.3**, The boundary conditions are

$$u(0) = 0$$

$$\left[\left(EA\frac{du}{dx}\right)\right]_{x=L} = P \tag{3.2}$$

The domain occupied by the rod is [0, L] along the real axis x.
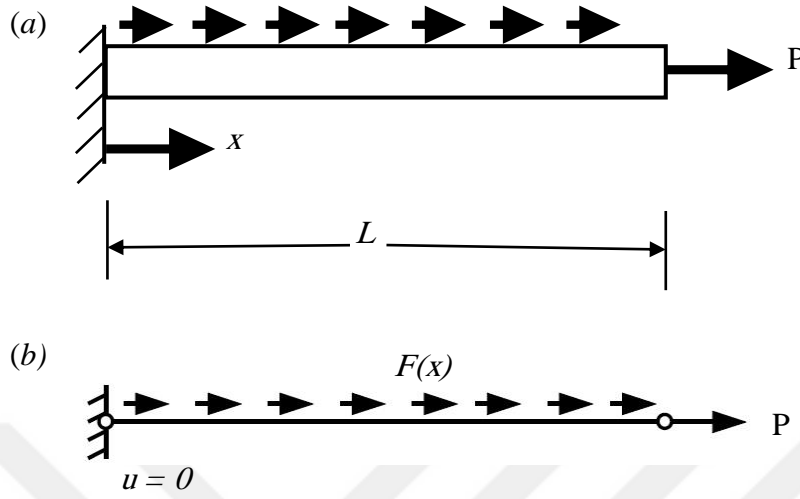
Figure 3.3: (a) physical rod model; (b) idealised rod model

3.4.2.1 Discretization and Element Equations

The next step is dividing the domain into discrete elements, then driving the element equations, using an integral form of the ODE, which is obtained by integrating the product of the ODE times a weight function υ as follows

$$0 = \int_{x_A}^{x_B} v \left[-\frac{d}{dx}\left(EA \frac{du}{dx} \right) - f \right] dx \tag{3.3}$$

This is called a weak form because the solution of $u(x)$ does not have to satisfy the ODE (3.1) for every infinite value of x in [0, L], in the strong sense. Instead, the ODE in (3.3) should be satisfied by the solution $u(x)$ only in a weighted average sense. So, it will be easier to find an approximate solution than an exact one. Although for a simple case like the rod, the exact solution is known, composite mechanics problems do not have an exact solution in most of the cases. The governing equation is obtained by integrating (3.3) by parts as follows

$$0 = \int_{x_A}^{x_B} EA \frac{dv}{dx}\frac{du}{dx} dx - \int_{x_A}^{x_B} vf dx - \left[v\left(EA \frac{du}{dx} \right) \right]_{x_A}^{x_B} \tag{3.4}$$

where $v(x)$ is a weight function, which is usually set equal to the primary variable $u(x)$. From the boundary, term can be concluded that

- specifying $v(x)$ at x_A or x_B is a basis boundary condition

- specifying $(EA\frac{du}{dx})$ at which end is the natural boundary condition
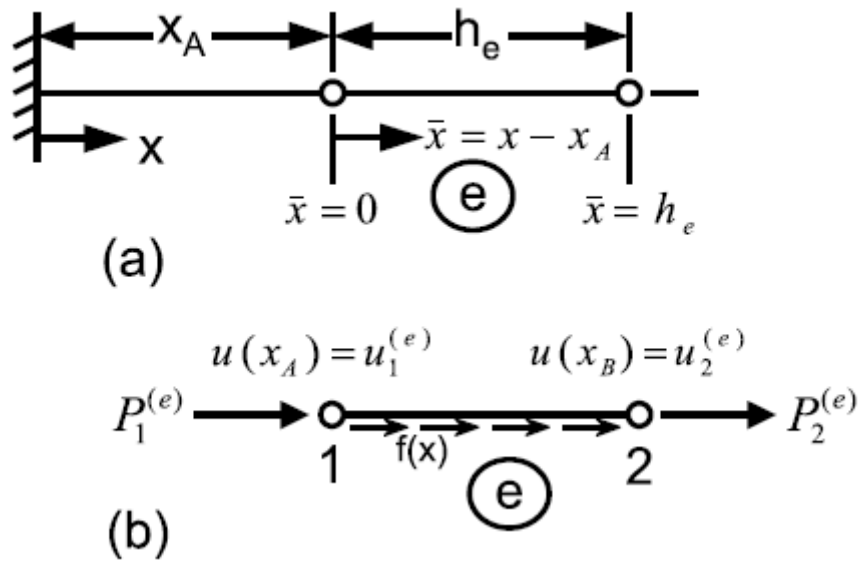
Figure 3.4: Discretization into elements [67]

while $u(x)$ is the main variable, $(EA\frac{du}{dx}) = EA\epsilon_x = A\sigma_x$ is the side variable.

Let

$$u(x_A) = u_1^e$$
$$u(x_B) = u_1^e$$
$$-\left[\left(EA\frac{du}{dx}\right)\right]_{x_A} = P_1^e \tag{3.5}$$
$$\left[\left(EA\frac{du}{dx}\right)\right]_{x_B} = P_2^e$$

Then, the governing equation becomes

$$0 = \int_{x_A}^{x_B} \left(EA \frac{dv}{dx} \frac{du}{dx} - vf \right) dx - P_1^e\, v(x_A) - P_2^e\, v(x_B) = B(u,v) - l(v) \quad (3.6)$$

with

$$B(u,v) = \int_{x_A}^{x_B} EA \frac{dv}{dx} \frac{du}{dx} dx$$

$$l(v) = \int_{x_A}^{x_B} vf\, dx + P_1^e\, v(x_A) + P_2^e\, v(x_B) \tag{3.7}$$

3.4.2.2 Approximation Over Element

After that, the unknown $u(x)$ is approximated as a series expansion of known functions $N_i^e(x)$ and unknown coefficient a_j^e, as

$$u_e(x) = \sum_{j=1}^{n} a_j^e N_j^e(x)$$

where a_j^e are the wanted coefficients and $N_j^e(x)$ are the interpolation functions. For the weight function $v(x)$, Ritz method can be used for the weight function $v(x)$, in which $v(x) = N_j^e(x)$. substituting in the governing Equation (3.6) results

$$\sum_{j=1}^{n} \left(\int_{x_A}^{x_B} EA \frac{dv}{dx} \frac{du}{dx} dx \right) a_j^e = \int_{x_A}^{x_B} N_i^e f\, dx + P_1^e N_i^e(x_A) + P_2^e N_i^e(x_B) \tag{3.8}$$

Which can be written as

$$\sum_{j=1}^{n} K_{ij}^e a_i^e = F_i^e \tag{3.9}$$

or as a matrix form

$$[K^e]\{a^e\} = \{F^e\}$$

(3.10)

where $[K^e]$ is the element stiffness matrix, $\{a^e\}$ are the element unknown parameters, and $\{F^e\}$ is the element vector equivalent force.

3.4.2.3 Interpolation Functions

It is convenient to choose the function that represents the unknown coefficients as the nodal displacement, that is $a_i = u_i$. For a two-node element extending in the interval $x_e \leq x \leq x_{e+1}$, the following linear interpolation functions can be used

$$N_1^e = \frac{x_{e+1} - x}{h_e}$$

$$N_2^e = \frac{x - x_e}{h_e}$$

(3.11)

where $h_e = x_{e+1} - x_e$ is the length. These interpolation functions fulfil the following conditions

$$N_1^e(x_j) = \begin{cases} 0 & if \quad i \neq j \\ 1 & if \quad i = j \end{cases}$$

(3.12)

$$\sum_{i=1}^{2} N_i^e(x) = 1$$

(3.13)
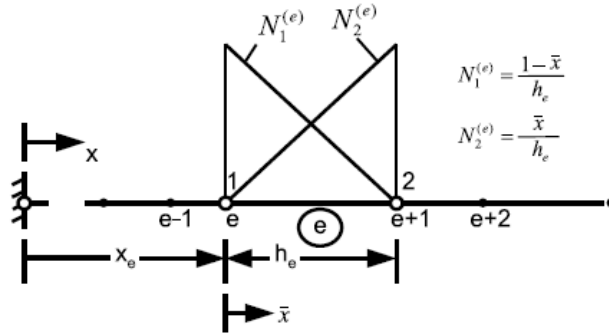
Figure 3.5: Linear interpolation functions for a two-node element rod [67]

Which ensure that unknown coefficients represent the nodal displacements,

i.e., $a_i = u_i$.

In general, more nodes per element imply more accuracy and less necessity for a fine mesh, but also imply higher cost in terms of computer processing time.

3.4.2.4 Element Equations for a Specific Problem

After interpolation, it is possible to rewrite (3.10) as

$$[K^e]\{u^e\} = \{F^e\} \tag{3.14}$$

where$\{u^e\}$ are the nodal displacement, $[K^e]$ is the element stiffness matrix given by

$$[N^e] = \begin{bmatrix} \int_{x_A}^{x_B} EA \frac{dN_1^e}{dx} \frac{dN_1^e}{dx} dx & \int_{x_A}^{x_B} EA \frac{dN_1^e}{dx} \frac{dN_2^e}{dx} dx \\ \int_{x_A}^{x_B} EA \frac{dN_2^e}{dx} \frac{dN_1^e}{dx} dx & \int_{x_A}^{x_B} EA \frac{dN_2^e}{dx} \frac{dN_2^e}{dx} dx \end{bmatrix} \tag{3.15}$$

and $\{F^e\}$ is the element force vector

$$[F_i^e] = \left\{ \begin{array}{c} \int_{x_A}^{x_B} N_1^e f \, dx + P_1^e \\ \int_{x_A}^{x_B} N_2^e f \, dx + P_2^e \end{array} \right\} \tag{3.16}$$

For a two-node rod element number e, the element length h_e, the constant cross-section area A_e and the modulus E are fixed. These values define the tensile-compression element stiffness as

$$k^e = \frac{EA_e}{h_e} \tag{3.17}$$

The distributed load f_e is the external loads on element, the force at number 1 is P_1^e and the force at end number 2 is P_2^e. Using these values, the interpolation functions (3.10), as well as (3.15) and (3.16), the element matrix stiffness and the equivalent nodal forces become

$$[K^e] = \begin{bmatrix} k^e & -k^e \\ -k^e & k^e \end{bmatrix} = \frac{EA_e}{h_e} \begin{bmatrix} 1 & -1 \\ -1 & 1 \end{bmatrix} \tag{3.18}$$

$$\{F^e\} = \frac{f_e h_e}{2} \begin{Bmatrix} 1 \\ 1 \end{Bmatrix} + \begin{Bmatrix} P_1^e \\ P_2^e \end{Bmatrix} \tag{3.19}$$
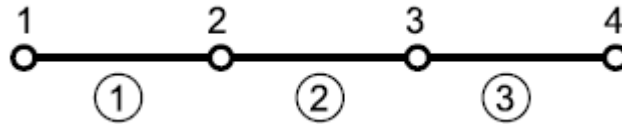
Figure 3.6: Connectivity between three two-node elements [67]

3.4.2.5   Assembly of Element Equations

The element unknown parameters coincide to displacements at the element nodes. Since a node must have the same displacement on both neighbouring elements, the value is unique. For example, using the connectivity of element demonstrated in Figure **3.6**, unique labels are assigned to the displacements, using capital letters. While a subscript indicates an element number, a subscript denotes a nodal number, as follow

$$u_1^1 = U_1$$

$$u_2^1 = U_2 = u_1^2$$

$$u_1^2 = U_3 = u_1^3$$

$$u_2^3 = U_4 \tag{3.20}$$

Up to now, the element equations can be written in the global system. First, the contribution of element number 1 is

$$\begin{bmatrix} k^1 & -k^1 & 0 & 0 \\ -k^1 & k^1 & 0 & 0 \\ 0 & 0 & 0 & 0 \\ 0 & 0 & 0 & 0 \end{bmatrix} \begin{pmatrix} U_1 \\ U_2 \\ U_3 \\ U_4 \end{pmatrix} = \begin{Bmatrix} f_1 h_1/2 \\ f_1 h_1/2 \\ 0 \\ 0 \end{Bmatrix} + \begin{Bmatrix} P_1^1 \\ P_2^1 \\ 0 \\ 0 \end{Bmatrix} \tag{3.21}$$

Then adding the contribution of element number 2 as follows

$$\begin{bmatrix} k^1 & -k^1 & 0 & 0 \\ -k^1 & k^1 & 0 & 0 \\ 0 & 0 & 0 & 0 \\ 0 & 0 & 0 & 0 \end{bmatrix} \begin{pmatrix} U_1 \\ U_2 \\ U_3 \\ U_4 \end{pmatrix} = \begin{Bmatrix} f_1 h_1/2 \\ f_1 h_1/2 + f_2 h_2/2 \\ f_2 h_2/2 \\ 0 \end{Bmatrix} + \begin{Bmatrix} P_1^1 \\ P_2^1 + P_1^2 \\ P_2^2 \\ 0 \end{Bmatrix} \tag{3.22}$$

Finally, to obtain the fully assembled system, element number 3 must be added as follows

$$\begin{bmatrix} k^1 & -k^1 & 0 & 0 \\ -k^1 & k^1 + k^2 & -k^2 & 0 \\ 0 & -k^2 & k^2 + k^3 & -k^3 \\ 0 & 0 & -k^3 & k^3 \end{bmatrix} \begin{pmatrix} U_1 \\ U_2 \\ U_3 \\ U_4 \end{pmatrix} = \frac{1}{2} \begin{Bmatrix} f_1 h_1 \\ f_1 h_1 + f_2 h_2 \\ f_2 h_2 + f_3 h_3 \\ f_3 h_3 \end{Bmatrix} + \begin{Bmatrix} P_1^1 \\ P_2^1 + P_1^2 \\ P_2^2 + P_1^3 \\ P_2^3 \end{Bmatrix}$$

$$\tag{3.23}$$

3.4.2.6 Boundary Conditions

The internal loads cancel whenever two elements share the same node due to equilibrium, or

$$P_2^1 + P_1^2 = 0$$
$$P_2^2 + P_1^3 = 0 \tag{3.24}$$

The remaining P_1^1 and P_3^2 are the forces at the end of the rod. If any end of the rod is fixed, then the displacement must be set to zero at that end. If the end at $x=0$ is fixed, then $U_1 = 0$ and the end at $x = L$ is free, then P_3^2 must be stated, since $U_4 \neq 0$. If it is not stated, then it is assumed that there is no force and set to be zero.

3.4.2.7 Solution of the Equations

The first row and column of the stiffness matrix are eliminated since the value of U_1 equals zero, a 3×3 system of algebraic equations is obtained, and solved for three unknowns: U_2, U_3, U_4. After finding the value of U_2, the reaction P_1^1 is computed from the equation of (3.23), as follows

$$P_2^1 + P_1^2 = 0$$
$$P_2^2 + P_1^3 = 0 \tag{3.24}$$

$$-k^1 U_2 = \frac{f_1 h_1}{2} + P_1^1 \tag{3.25}$$

Now, the U_i at 4 points along the rod is available. The next step is computing the solutions at any x can be done by interpolating with the interpolation functions, as follows

$$U^e(x) = \sum_{j=1}^{2} U_j^e N_j^e(x) \tag{3.26}$$

28

3.4.3 FEM Modelling of Microvascular Channels

Many inspiring works in the literature have discussed the effects of microvascular channels in the composite structure using FEA modelling. Most of them considered a simple orthogonal stacking order [68]; and plane strain assumption (i.e. 2D) [33], this work consists of a more general 3D model with considering various orthogonal stacking order, analysing various vascular shape and diameter will be included also in this work. Huang et al. [33] performed finite element analysis as a plain strain model on crack initiation and failure under load and validated their FEA results with experimental results by high-speed photography. Their FEA predicted that, crack initiation stress is 60-70% of final failure; while experimental crack initiation 70-80% of failure strength. Darren et al. [69] tried a different approach considering fully three-dimensional representative volume element (RVE) with general periodic boundary conditions for arbitrary layups, including quasi-isotropic configurations. They reported that, the channel orientation to the local fibre direction has no noticeable effect on the strength under combined load. Soghrati et al. [52] executed a computational analysis by means of Interface-enriched Generalized Finite Element Method (IGFEM) on 3D microvascular woven composite fin specimen to amplify its effectiveness in actively-cooling applications. They mainly focused on enhance the maximum temperature, void volume fraction and flow efficiency. They extended their work using stabilised IGFEM on straight and sinusoidal embedded microchannel structures. Stabilised IGFEM enabled them to study the pressure drop in the microchannels, the maximum allowable temperature of the coolant, and maximum temperature of the composite [53].

In the present study, a more generic 3D model is constructed to analyse the parameters of microvascular channels. The necessity of 3D model comes from the fact that the microchannel is opened along the longitudinal direction of the sample. This 3D model also overcomes the limitations of previous 2D models such as the boundary conditions and stacking conditions. In the next chapter, this 3D model is constructed first as a 3D representation of the model in Huang et al. model [33] for validation. After that, the model is regenerated for the present sample configuration to analyse the effects of the parameters in microchannels.

CHAPTER FOUR

MODEL DEVELOPMENT

4.1   Introduction

In this chapter, the development of the models used in this thesis are presented. In order to verify the correct configuration for the model generation, initially a 3D version of a previous model in the literature is generated and the results are compared. The model in Huang et al. [33] was selected for this purpose as it has similar configuration in terms of microvascular channels compared to our present study. This plain strain model is regenerated as 3D for these purposes. First, with 2D model, it is not possible to study laminates with different angles. Second, the tensile load in the longitudinal direction is studied. Third, 3D model is much more flexible to further studies including various other types of loading such as bending. After verification, the present sample model is regenerated similar to the validation model but with different stacking configurations and dimensions according to the manufactured samples in UTAA. Finally, the results of the new model are analyzed to investigate the effect of manufacturing parameters on the structure.

4.2   Finite Element Model Development of the Validation Model

4.2.1   Geometrical and Material Model

The geometry of the validation model is presented in Figure **4.1** and listed in Table **1** which was constructed according to the micrograph images in Huang et. al. [33]. In this model, a vascule diameter of 0.4mm was considered. The default length of the models is 50r, which is long enough to avoid any unnecessary boundary effects. This issues was also considered while modelling the present sample model. For this vascule diameter, the length (L) is defined as 5mm. The resin pocket length (L_{RP}), the disturbance height (h_d), and fibre disturbance angle (θ_d) are obtained from the micro-scale pictures of the specimens and normalized by the radius (r). The laminate consists of 24 plies of UD IM7/8552. Each layer thickness is 0.125mm. Fibre direction is set

to be orthogonal to the vascular hole direction. Only one quarter of the specimen is presented due to the symmetry in geometry and boundary conditions. In the 2D model, there was no need to put the width of the laminate as the model was plane strain. However, in 3D model, the width of the laminate should be specified. This value should be specified large enough to prevent stress concentrations when longitudinal loading is applied and edge effect but small enough to decrease computational speed. The width is taken as 4 mm after performing various trial analysis with the model. The mechanical and thermal properties of IM7/8552 composite laminate and the resin (Hexcel 8552) are given in Table **2** and Table **3**, respectively.
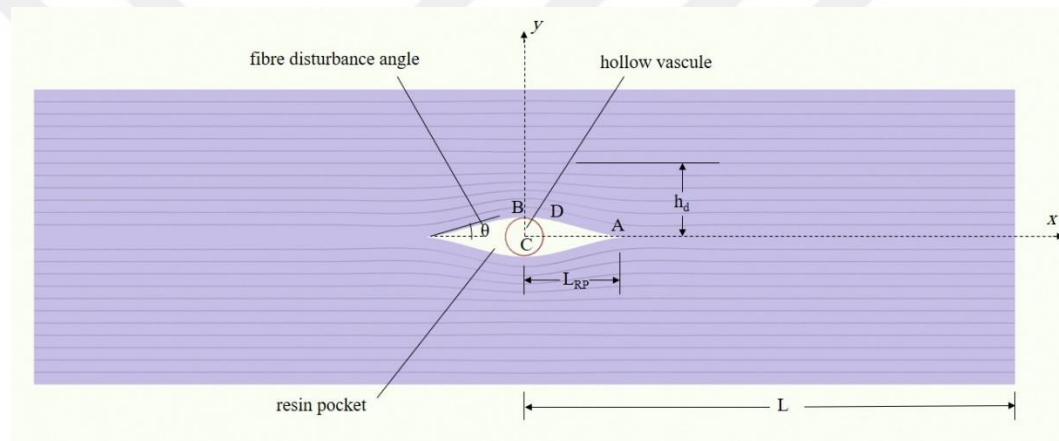
Figure 4.1: The model of laminate with embedded circular vascule surrounded by a resin pocket

Table 1: Geometric parameters of circular vascule [33]

Vascule diameter (mm)	Resin pocket length (L_{RP-} mm)	disturbance height (h_d- mm)	fibre disturbance angle (θ_d)	resin pocket area, A (μm^2)	lay-up system
0.4	1.016	0.742	9.85°	3.96 x 10^5	24 plies unidirectional

Table 2: Mechanical and thermal properties of IM7/8552 composite [33]

Young's Modulus (GPa)		Shear Modulus (GPa)		Poisson's Ratio		Thermal coefficient (K^{-1})	
E_{11C}	145	G_{12}	5.12	υ_{12}	0.3	α_{11}	6.0 x 10^{-7}
E_{22C}	10.20	G_{23}	5.12	υ_{23}	0.487	α_{22}	2.86 x 10^{-5}
E_{33C}	10.20	G_{13}	3.92	υ_{13}	0.3	α_{33}	2.86 x 10^{-5}

Table 3: Mechanical and thermal properties of Hexcel 8552 neat epoxy (resin) [33]

Young's Modulus (GPa) E	Poisson's Ratio υ_{12}	Thermal coefficient (K^{-1}) α
4.67	0.35	5.0×10^{-5}

4.2.2 Boundary Conditions and Load

Symmetry boundary conditions are applied at x-z and y-z planes where the hole exists. A compressive load (i.e. pressure) of 1.65 GPa (σ_0) is applied on the y-z plane at (x=5mm) equal to symmetric boundary condition is applied. The curing effect (i.e. curing) also included the 3D model as two predefined fields, The initial temperature is taken as (150°C) and cooled down to (20°C) as the second predefined field temperature. Figure **4.2** shows the boundary conditions of the validation model.
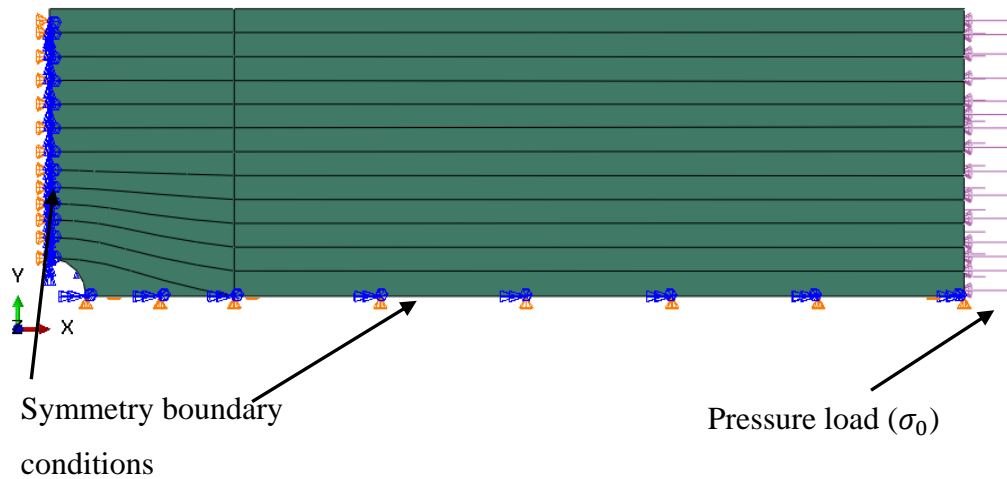
Figure 4.2: Boundary conditions and load for the FEA model

4.2.3 Elements and Mesh

The 2D FE model in [33] was meshed with plain strain quadrilateral elements (CPE8) while due to its 3D nature, the present model is meshed with 8-node Linear 3D elements (C3D8) in FE code ABAQUS/Standard. The regions of interest had the finer mesh and it is located around the hole (the resin pocket and the curved layers). The numbers of nodes/elements for each region is (1) 4554/3390, (2) 17556/15552, (3) 31812/28224. (Figure **4.3**)
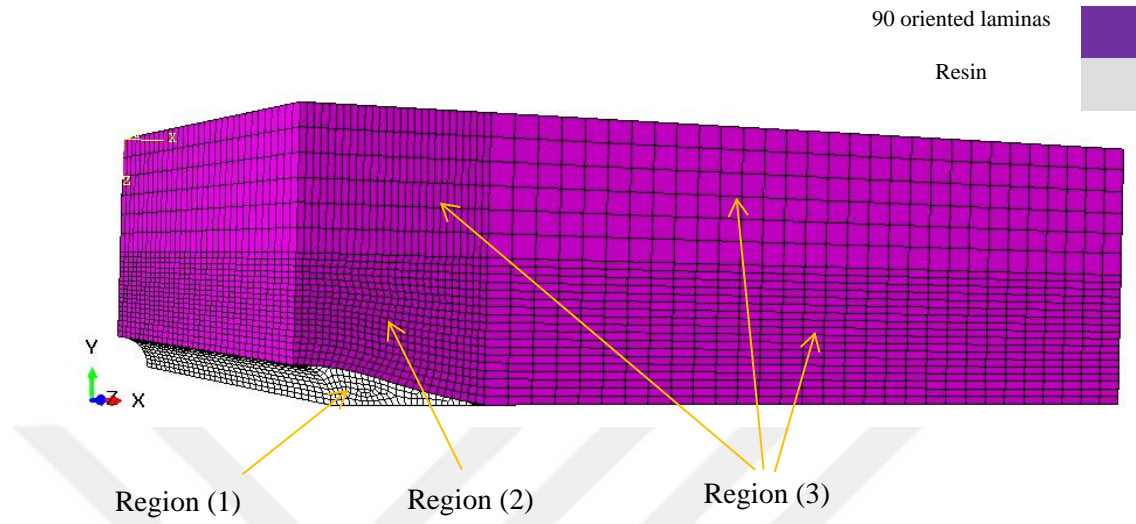
Figure 4.3: Quarter section of the 3D FEA model meshed with 8-node Linear 3D elements (C3D8) (The readers are referred to soft version of the thesis for clarity)

4.3 Parametric Model for Present Samples

4.3.1 Introduction

As mentioned in the previous section, the 3D models are generated based on the samples being prepared in UTAA. The aim is to investigate the mechanical behavior under tensile load so it was decided to prepare the samples according to ASTM-D 3039 "Standard Test Method for Tensile Properties of Polymer Matrix Composite Materials". The parameters such as stacking conditions and vascule geometry of the present 3D model are varied to investigate their effect on the stresses.

4.3.2 Geometrical Configurations

In order to determine the geometrical configuration near the vascules, two samples were prepared with different stacking conditions. One is $[90/0]_{4s}$ and the other is $[0/90]_{4s}$. Resin-rich pocket dimensions, height of the disturbed fibers and fibre disturbance angle were taken directly from the specimen using micro-capturing

camera (Veho vms-004). The micro-pictures of each specimen are shown in Figure **4.4** and Figure **4.5** which reveal the area around vascule. There is a significant difference between these two-stacking orders in the matter of resin-rich pocket dimensions. The specimens with fibers oriented parallel to the vascule [90/0]$_{4s}$ has a much smaller resin-rich pocket than the ones with fibres orthogonal to the vascule [0/90]$_{4s}$, similar findings are observed in [32, 68] as well in which the local orientation of midplane fibers relative to an embedded channel impacts directly on the geometrical configuration. The waviness in the laminate and the resin-rich pocket can also be observed from the images similar to the previous studies [33, 37, 68]. The tensile tests for the both stacking sequence [0/90]$_{4s}$ and [90/0]$_{4s}$ specimens expected to show that the [90/0]$_{4s}$ would have a higher mudulus of elasticity because of the resin-rich pocket size being larger in [0/90]$_{4s}$.
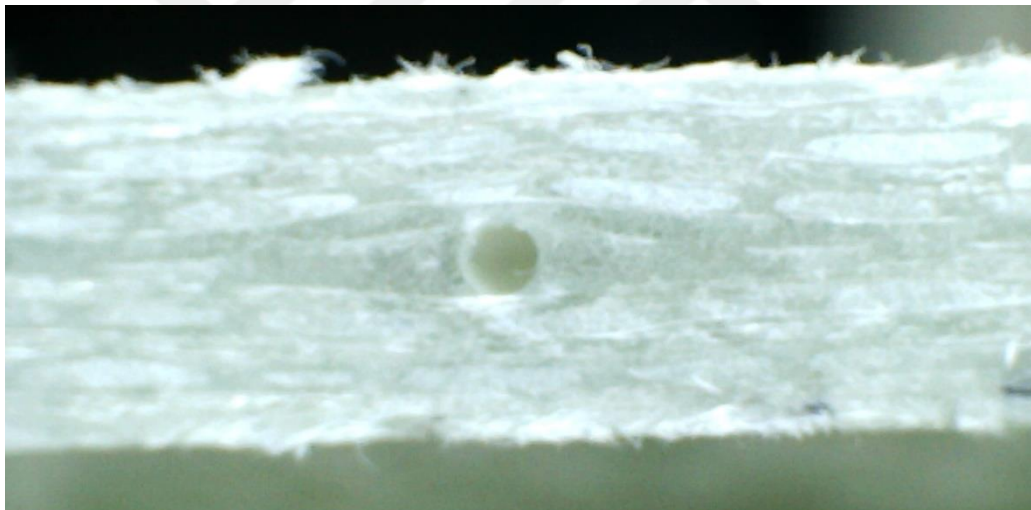
Figure 4.4: Micro-picture for a [0/90]$_{4s}$ GFRP sample embedded with vascule diameter of 1mm
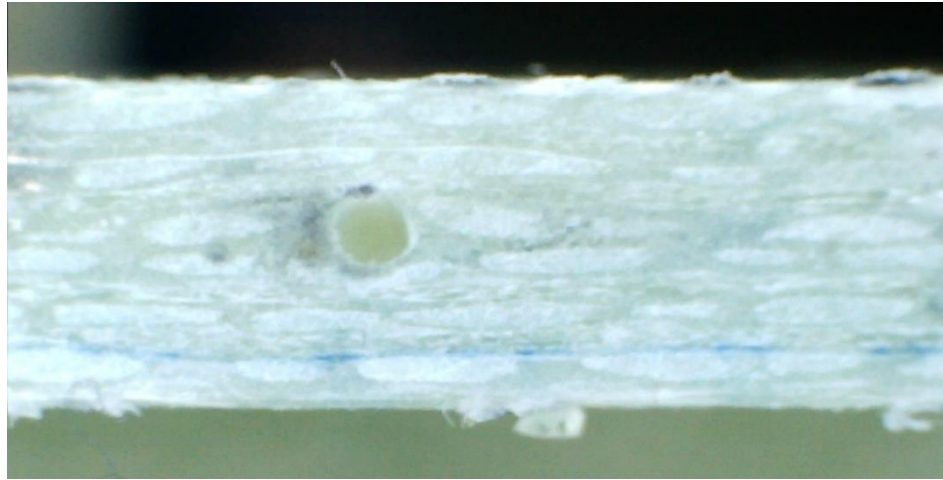
Figure 4.5: Micro-picture for a [90/0]$_{4s}$ GFRP sample embedded with vascule diameter of 1mm

The dimensions obtained from the micro-images and the parameters considered in this study are presented in Table **4**. In addition to circular, elliptical configurations of channels were also investigated to see their effects. The length, and the disturbance height of the resin-rich pocket for vascule diameters smaller than 1 mm are scaled accroding to their diameter while taking the vascule diameter of 1 mm as the reference. Stacking sequences considered in the study are [90/0]$_{4s,}$ [0/90]$_{4s}$. In addition, UD 0 and UD 90 models are prepared in order to observe the effects of stacking direction on the stress distribution

Table 4: Geometric parameters of circular vascule for the present samples

Vascule diameter (mm)	Resin-rich pocket length (mm) (L$_{RP}$)	disturbance height (mm) (h$_d$)	fibre disturbance angle (θ_d)	Vascule shape	lay-up system
1	1.8	0.95	16°	Circular	16 plies
1	3.274	1.461	10°	Circular	16 plies
0.8	2.593	1.4437	9°	Circular	16 plies
0.6	2.139	1.15875	8°	Circular	16 plies
0.4	1.56877	0.8756	8°	Circular	16 plies
1st ellipse 1.111 x 0.9	3.1274	1.45	9°	Elliptical	16 plies
2nd ellipse 0.9143 x 0.7	2.142	1.4175	10°	Elliptical	16 plies

The elliptical models are assumed to have the same cross sectional area with the vascule diameter of 1mm and 0.8 mm. and assuming the minor diameter to be 10% smaller than the orignal diameter.The major diameter using the equaition $a = \frac{d^2}{b}$, where *a* refers to the major diameter of the ellipse, and *b* refers to the minor diameter in the ellipse as shown in Figure **4.6**. The models are prepared for only 1mm and 0.8mm vascule diameters only, because modeling the elliptical version of the vascule channels with e smaller diameter results in neglegible diffrences between *a* and *b*.
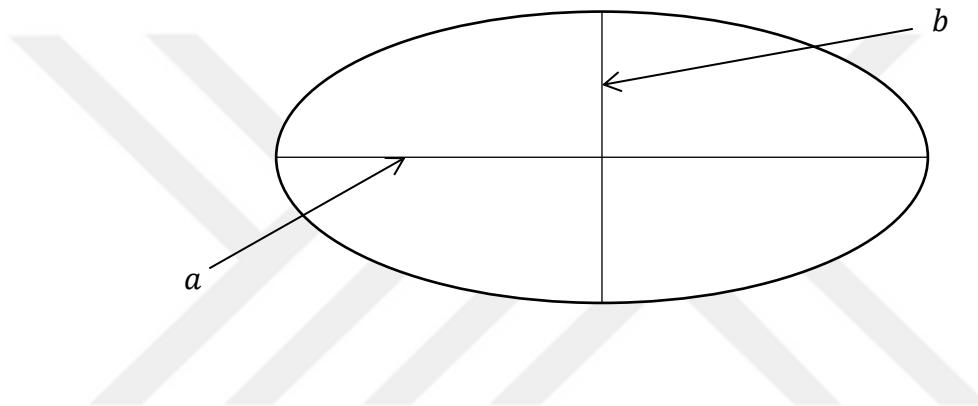
Figure 4.6: Ellipse dimensions

4.3.3   Finite Element Model of the Parametric Model

According to the ASTM standards (D 3039) for in-plane tensile properties of polymer matrix composites reinforced by high modulus fibers, the specimen dimensions should be 250x25mm and the thickness for the test sample is taken as 4.5mm (Figure **4.7**). The sizes in the standards are given considering the experimental issues such as to prevent stress concentrations from the tabs. Trial analyses showed that a specimen of this length requires a lot of computational power. Also, a fine mesh is needed in the regions near the vascule and when the model is too large there is a great chance of element distortion. Therefore, the length for the model is scaled by 1:10 of the real specimen in the rest of the study which is equal to 25mm. Similar to the validation model, only one quarter of the real specimen section is modeled due to the symmetry (Figure **4.8** and Figure **4.9**). The details around the micro vascule are shown in Figure **4.10** for the configuration of vascule diameter of 1mm. An extra study is performed

to verify the results of the small-scale model which should be similar to the results of the model with real specimen dimensions.
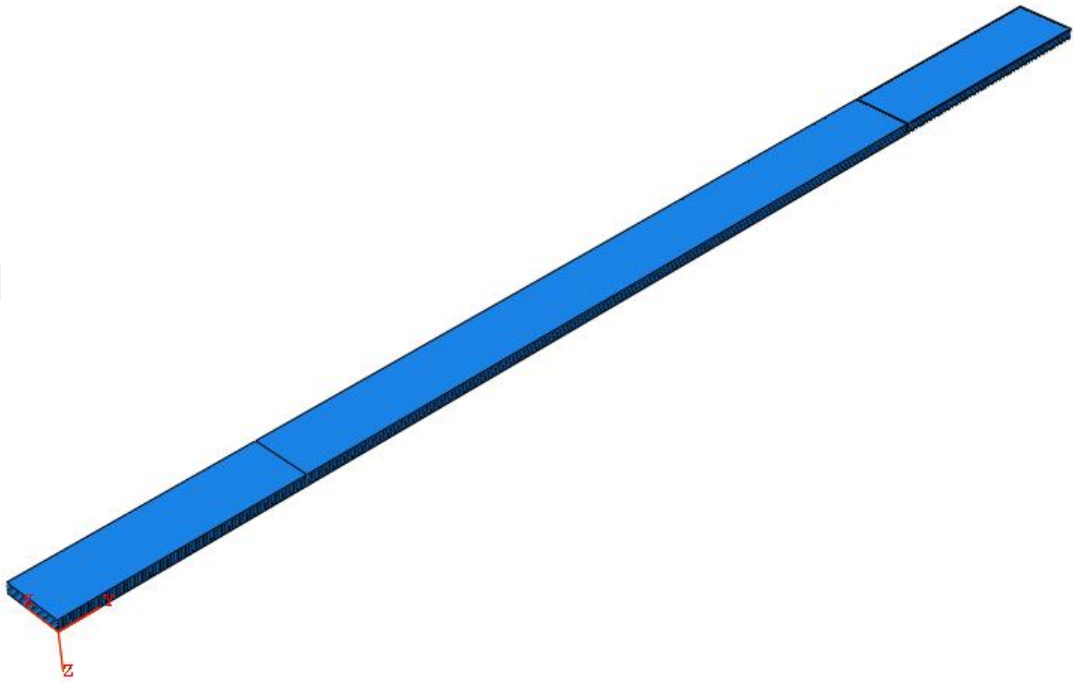
Figure 4.7: Quarter section of 3D full model of the GFRP tensile test specimen
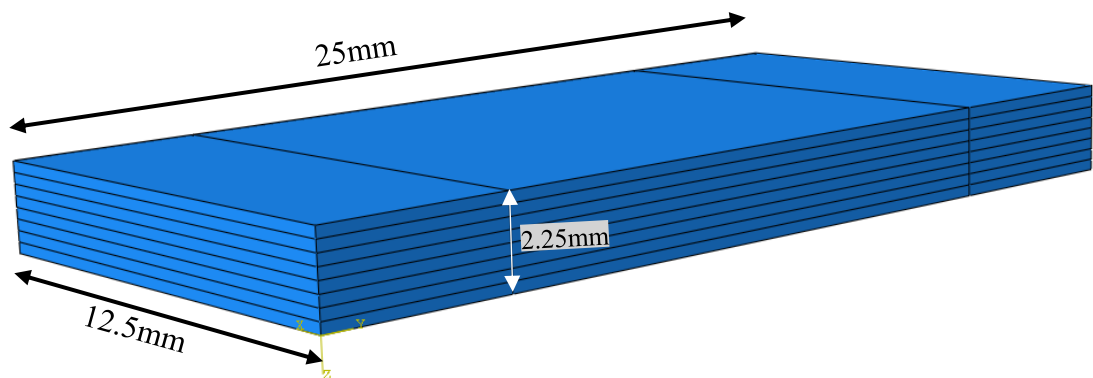
Figure 4.8: Quarter section of 3D scaled model of the GFRP specimen with the dimensions of the model used in this study
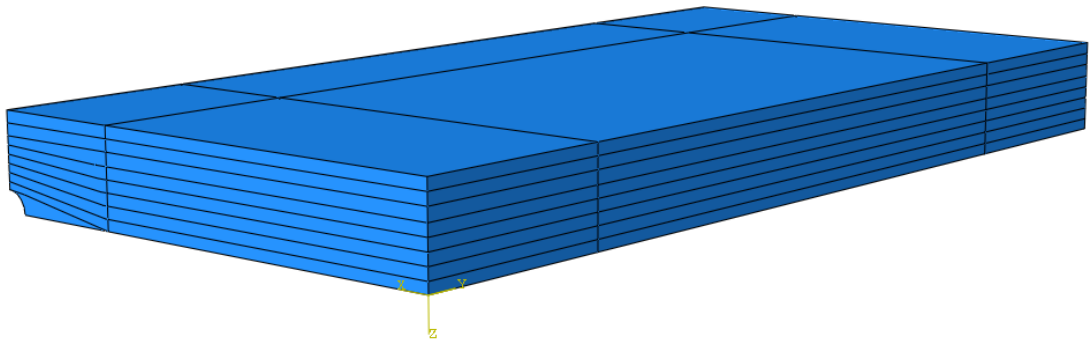
Figure 4.9: Quarter section of 3D scaled model of the GFRP specimen with 1mm microchannel
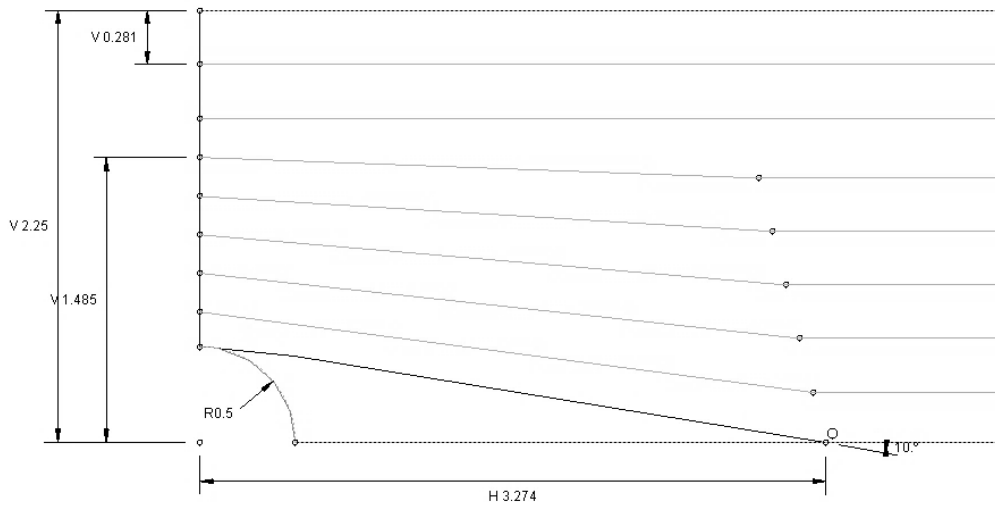
Figure 4.10: Resin-rich pocket dimensions for the configuration of vascule diameter of 1 mm

4.3.4 Material and Properties

The material used is E-Glass/Aradur-564: Araldite 2954 with 55% volume fraction. The E-Glass fibre properties was taken from [70] and resin Ardur-564: Araldite 2954 was taken from the supplier's data and listed in Table **5**, and Table **6** respectively.

Table 5: Material properties for E-Glass fibre [70]

Young's Modulus (GPa)	Poisson's Ratio
73.35	0.22

Table 6: Material properties for resin Ardur-564: Araldite 2954 [71]

Young's Modulus (GPa)	Poisson's Ratio
2.5	0.35

The material properties for the E-Glass/Ardur-564:Araldite 2954 lamina are calculated using the mixture rule given for classical laminate theory [3]. In order to determine these orthotropic constants, following calculations are performed:

$$E_{11} = (1 - VF)E_m + VF.E_f \tag{4.1}$$

$$E_{22} = E_{33} = \frac{E_m.E_f}{(1 - VF)E_f + VF.E_m} \tag{4.2}$$

$$v_{12} = v_{13} = (1 - VF)v_m + VF.v_f \tag{4.3}$$

$$v_{21} = \frac{E_{22}}{E_{11}}v_{12} \tag{4.4}$$

$$v_{23} = \frac{v_{12}(1 - v_{21})}{1 - v_{12}} \tag{4.5}$$

the shear modulus G is calculated using Equation (2.1) for both fibre G_f and matrix G_m then implemented in the Equations (4.6) to get G_{12} and G_{13}

$$G_{12} = G_{13} = \frac{G_m.G_f}{(1 - VF)G_f + VF.G_m} \tag{4.6}$$

and finally, G_{23} is computed as follows

$$G_{23} = \frac{E_{22}}{2(1 + v_{23})} \tag{4.7}$$

The calculated material properties for E-Glass\Ardur-564 are listed in Table **7** for 55% volume fraction. Assigned material sections are given in Figure **4.10**.

Table 7: Material properties for 55%VF E-Glass/Ardur-564: Araldite 2954 unidirectional lamina

Young's Modulus (GPa)		Shear Modulus (GPa)		Poisson's Ratio	
E_{11}	40.917	G_{12}	1.982	υ_{12}	0.2785
E_{22}	5.33	G_{23}	1.942	υ_{23}	0.37
E_{33}	5.33	G_{13}	1.932	υ_{13}	0.2785

90 oriented laminas

0 oriented laminas

Resin

Figure 4.11: Material sections assignment

4.3.5 Boundary Conditions and Loading

The boundary conditions are shown in Figure **4.12**. The model is divided into 3 sub-sections. The first section is the fixed grip which has a length equal to one fifth of the whole model length, and fixed in all directions (U1=0, U2=0, U3=0). The second section is the zone between the grips. The third section is the moving grip with length equal to the fixed grip, a displacement BC in the U3 direction is applied to this grip to give a 0.1% strain as this is accomplished by multiplying 0.1% strain with the length between the grips. In addition to the gripping boundary conditions, there are two symmetric boundary conditions about the *x-axis* and the *y-axis* due to model being symmetric quadratically.
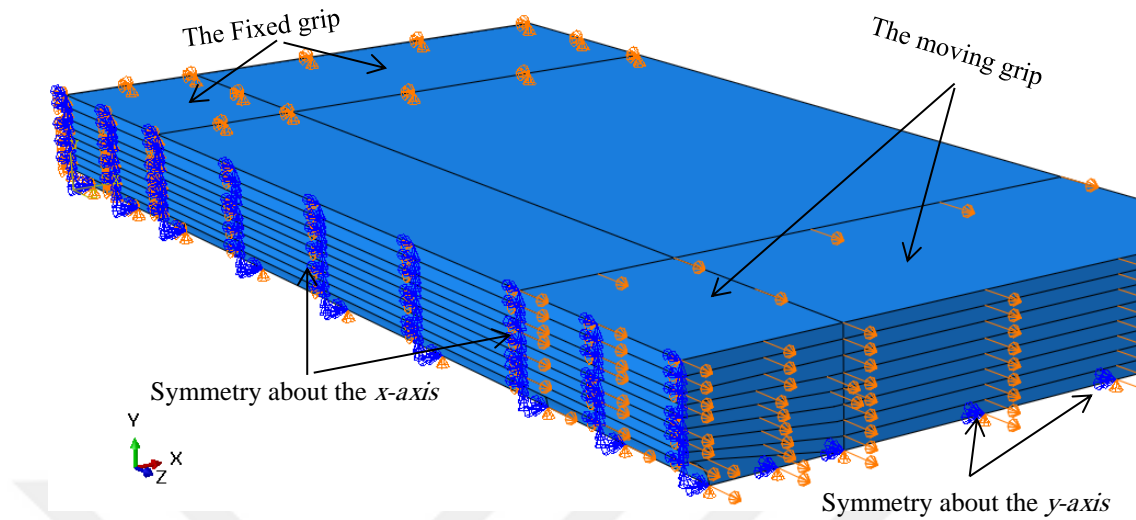
Figure 4.12: Boundary conditions of the FEA model

4.3.6 Elements and Mesh

The meshing style is selected as similar to the validation model as the results with such elements produced promising results. The present model of 1mm vascule diameter as an example is meshed with 40600 8-node Linear 3D elements (C3D8) similar to the validation model. There are three distinguished regions as displayed in Figure **4.13**, the resin-rich pocket and it is meshed with 5600 elements. The second region is the lamination above the resin-rich pocket, it is divided in order to give it a finer mesh than the third region. The number of elements in the second region are 17450 elements. The third region is meshed with 17550 elements. As observed in Figure **4.13**, coarser mesh is assigned to this region compared to the other regions as this region is far from the microchannel and hence, the area of interest. [72].
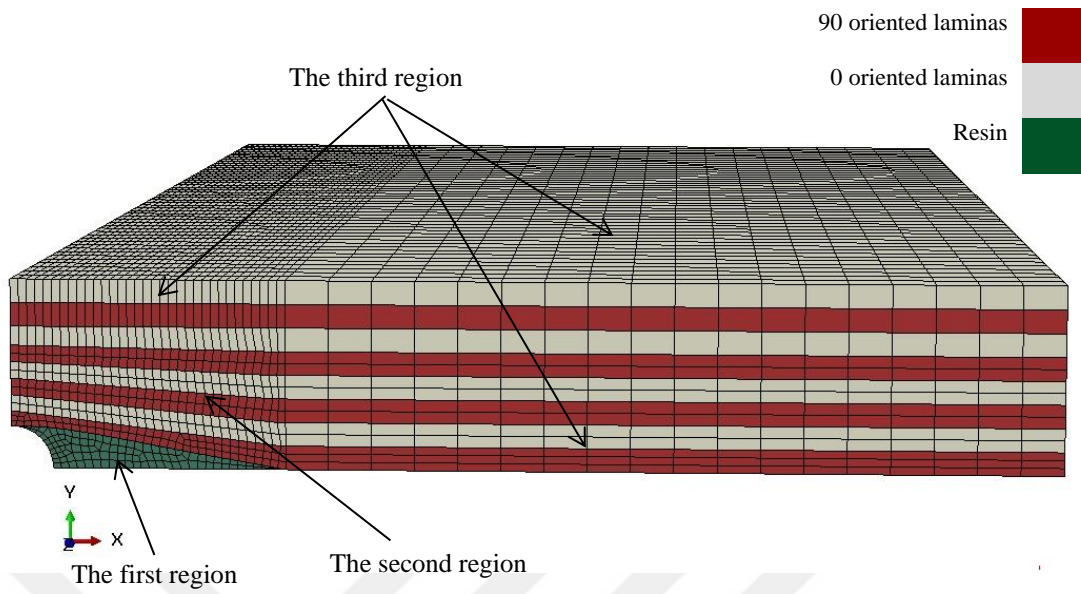
Figure 4.13: Quarter section of a 3D FEM model meshed with 8-node Linear 3D elements (C3D8)

CHAPTER FIVE

RESULTS AND DISCUSSION

5.1   Introduction

In this chapter, all the results obtained by the models introduced in the previous chapter are presented. First, the results of the 3D verification model are compared with the results obtained in [33] which includes the effect of thermal stresses Then the results of the present model are given. These starts with the comparison of the longitudinal stress contours for the scaled model versus the real model. Then the results of the case studies are presented. These include the stress vs distances in the resin pocket and stress distribution contours for various vascular diameters, shapes and various lamination sequences mentioned in the previous chapter. Finally, the obtained results are discussed.

5.2   Results of the Validation Model

In this section, graphical results and stress contours for the 3D model are compared with the results given in the plane strain model [33]. The results for the 3D model is extracted from the mid-section of the model as displayed in Figure **5.1**.
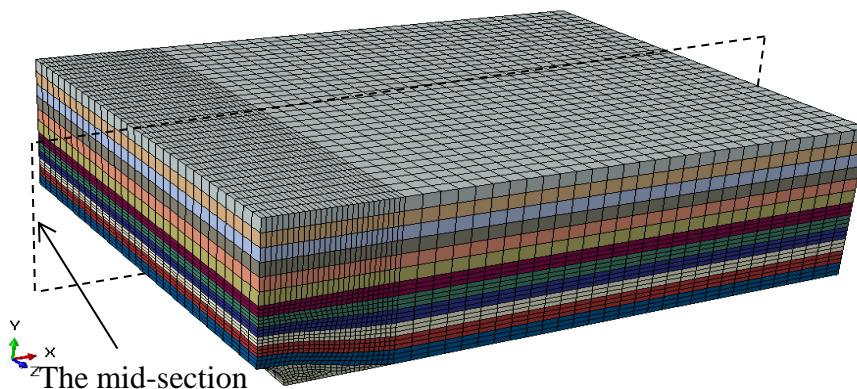
Figure 5.1: The mid-section position on 3D model
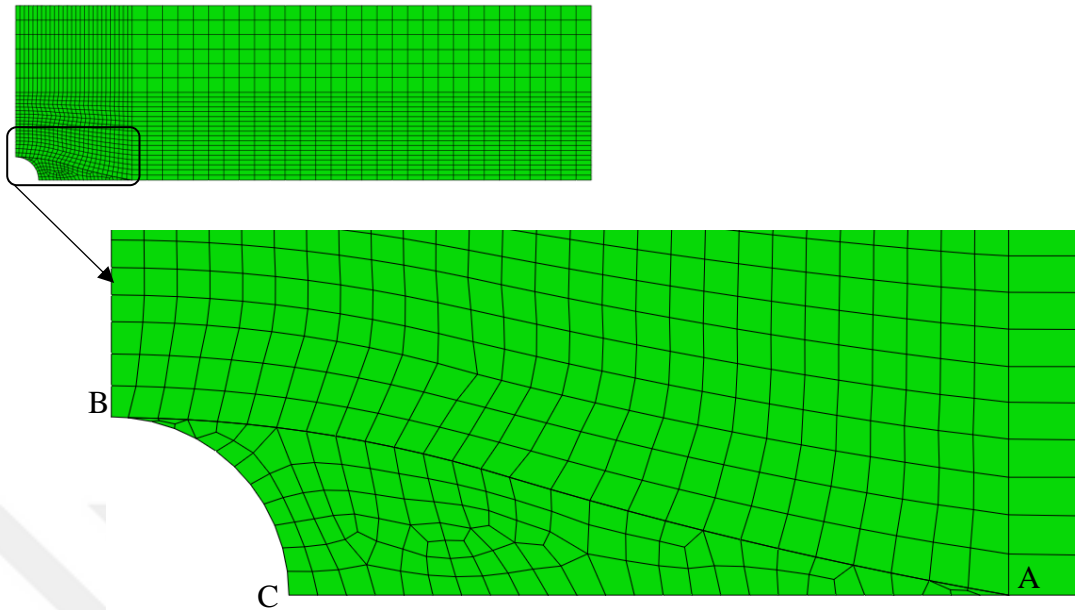
Figure 5.2: Zoomed section of the resin-rich pocket mesh

The variations of stresses along in the resin pocket are presented in Figure **5.3**. The points A, B, C, and D were pointed out in Figure **4.1** in the previous chapter. The *y-axis* indicates the SCF (or normalized stress) calculated by one of the stress components divided by the average applied stress (σ_o=1.65 GPa) The *x-axis* of the graphs in Figure **5.3** and Figure **5.4** is shown as a normalized distance from the vascule centre through points C and A to the end of the model at (x =5mm). While in Figure **5.5** the *x-axis* represents the normalized distance from point B which located above the vascule through point D to point A.

Figure **5.3** shows the normalized stress in the *x*-direction along the resin. Very similar behaviour for the normalized stress component σ_x/σ_o is observed for the 3D model compared with the plane strain model. Both of (a) and (b) plots have a very low longitudinal stress value at the resin pocket region. The stress increases rapidly in the composite region due to the significant difference in the material stiffness, until reaches the maximum value at the end of the models (x=L).
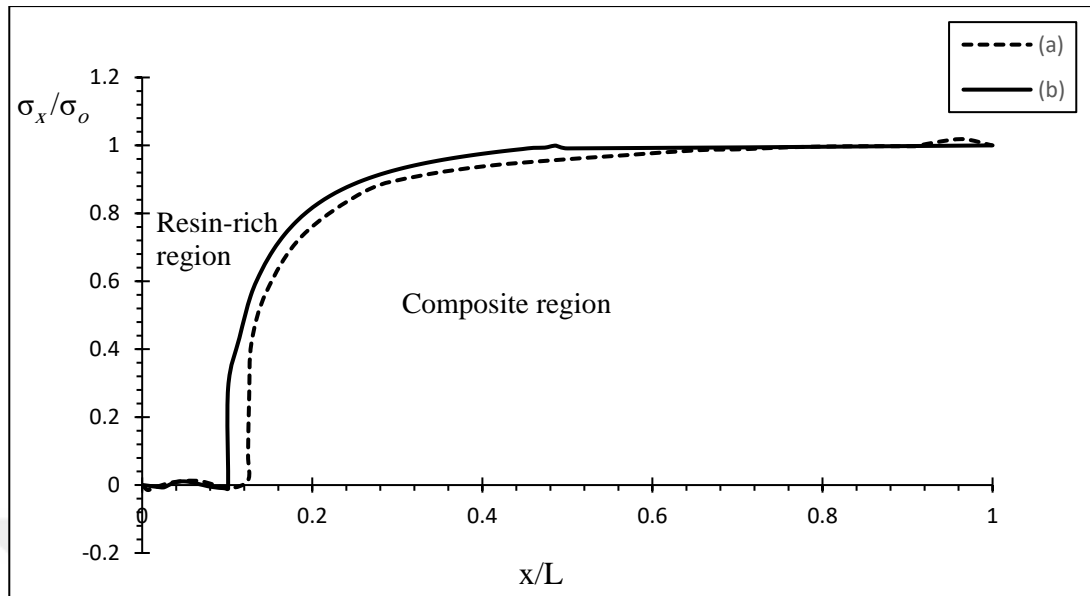
Figure 5.3: Normalized σ$_x$ along the *x-axis* for (a) 2D plain strain model [33]; (b) present 3D model

Figure **5.4** shows the distribution of the normalized stress in the *y*-direction. Similar behavior was observed for both cases in this figure as well. The only difference is near to the region at point A. This is the point where the resin pocket ends and the composite starts. Highly distorted triangular elements are present at that region (Figure **5.2**). Thus, the stresses at these regions are not realistic and may vary for different models. This much of variances are expected since the 3D model has some different characteristics compared to 2D model including mesh numbers, and element types. The normalized stress values are very low compared to the results presented in Figure **5.3** as these are transverse stress concentrations. Thus, the relative difference between the models looks relatively larger. Nevertheless, a similar trend was observed for the models. The results correspond to the findings of Shivakumar & Bhargava [73] as well.
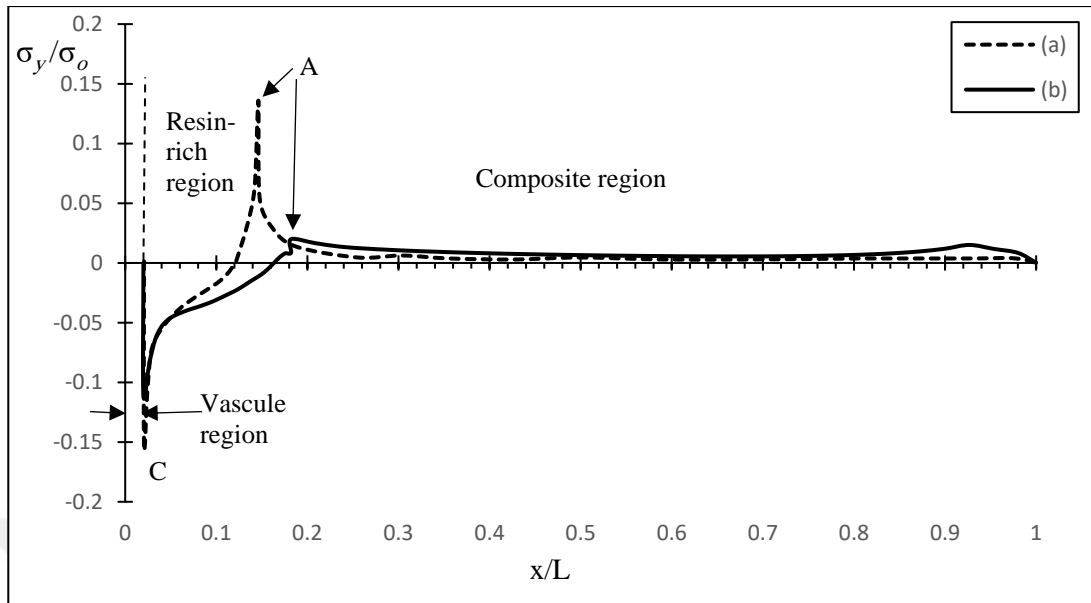
Figure 5.4: Normalized σ*y* along the *x-axis* for (a) 2D plain strain model [33]; (b) present 3D model

Figure **5.5** shows the relation between the normalized stress component σ_y/σ_o to the normalized curved path (BDA). Similarly to Figure **5.4**, the stress concentrations are different only near point A.
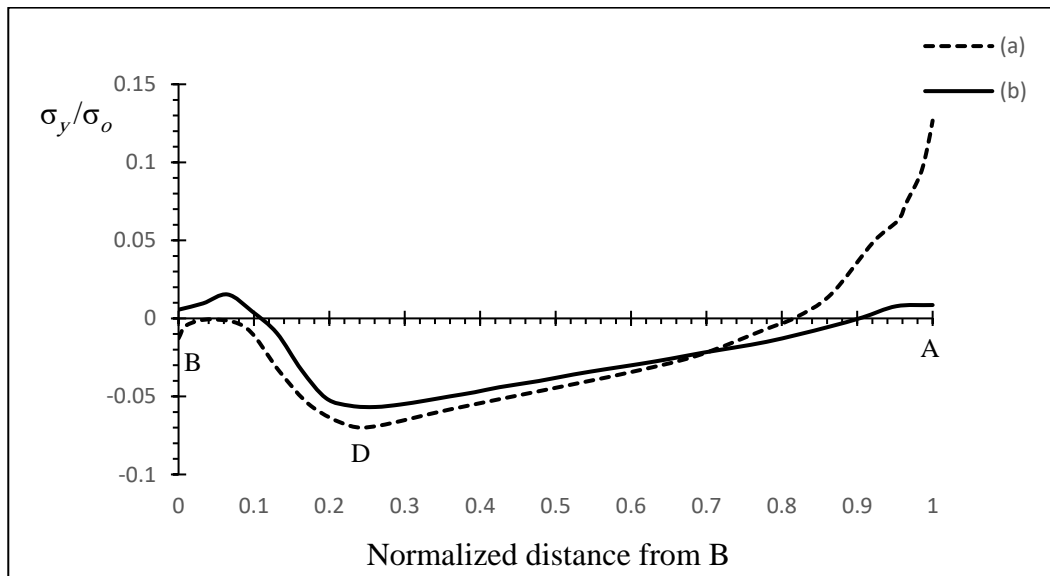
Figure 5.5: Normalized σy along the normalized curved path (BDA): for (a) 2D plain strain model [33]; (b) present 3D model

Figure **5.6** and Figure **5.7** illustrate the stress and strain contours for both models. Apparently, the contours look quite similar. In both models, the maximum transverse tensile stress and strain are observed near to point C and the maximum longitudinal compressive stress and strain are observed near point B.
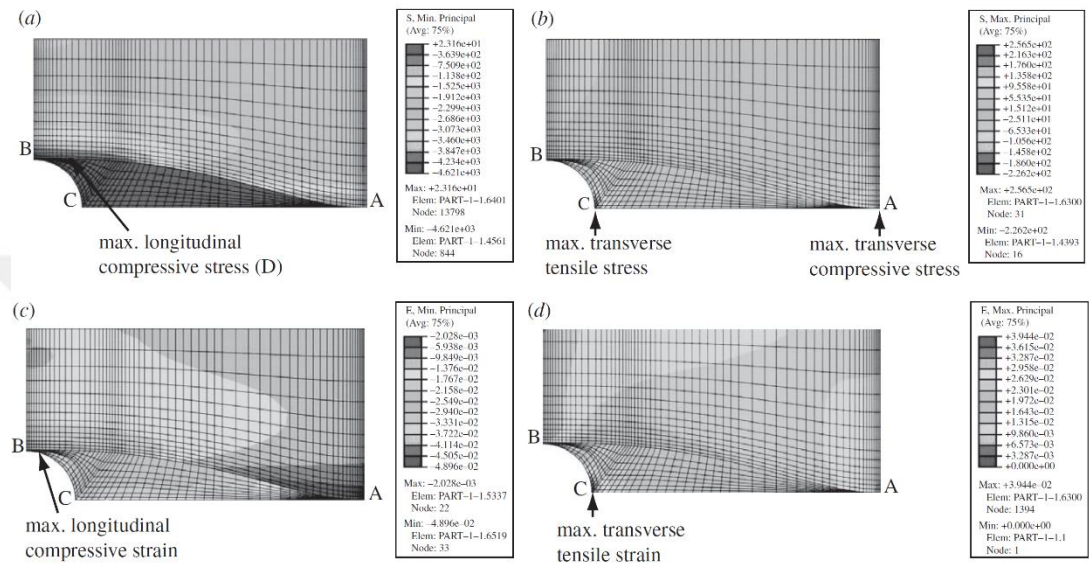
Figure 5.6: (a) longitudinal stress contour; (b) transversal stress contour; (c) longitudinal strain contour; (d) transversal strain contour, around vascule diameter of 0.4 mm, for the model presented in [33]
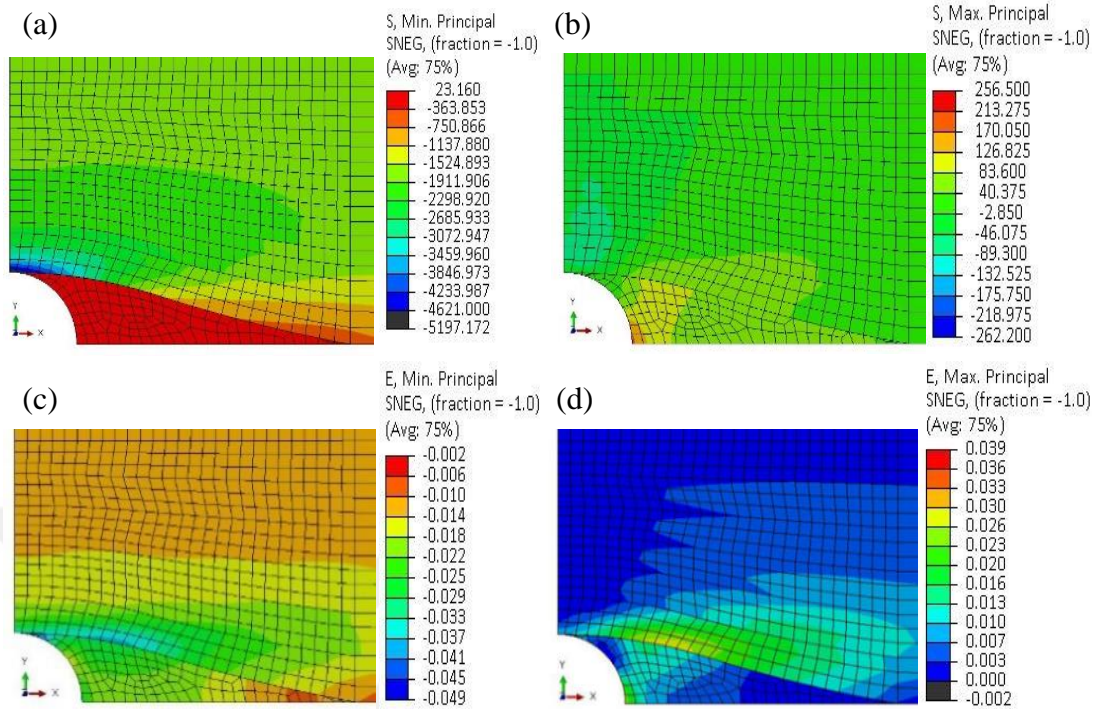
Figure 5.7: (a) longitudinal stress contour; (b) transversal stress contour; (c) longitudinal strain contour; and (d) transversal strain contour, around vascule diameter of 0.4 mm, for 3D model

According to the plots above, the results between the developed 3D model and 2D model given in [33] are considered similar enough to each other. Therefore, the 3D model is validated and can be utilised to apply different boundary conditions and stacking configurations.

As mentioned in Chapter 4, the effect of curing was also included in [33], so as the validation model. An extra study was performed to observe how much effective the curing cycle is as it cooled down from 150 C to 20 C. Figure **5.8** and Figure **5.9** display the longitudinal and transversal stress contours for the validation model with and without curing effect. The distributions show an insignificant difference due to the curing effect. For this reason, the curing effect is not considered for the present sample models. Another reason for the curing effect to be excluded is to avoid the coupling effect in the stress results and to observe solely the effects of other parameters.
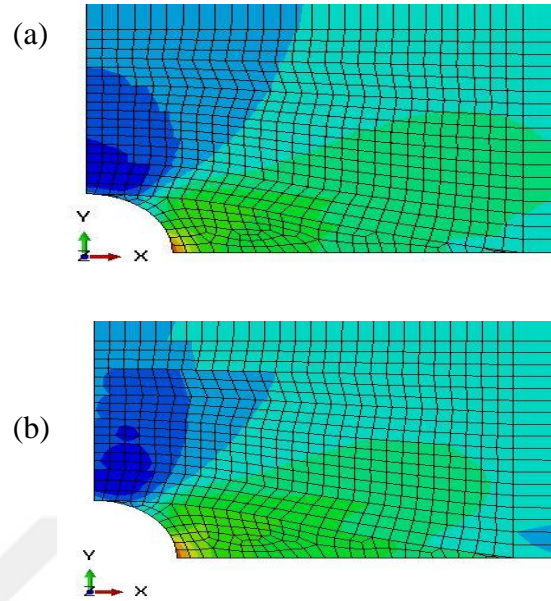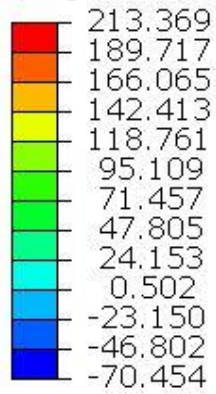
Figure 5.8: Longitudinal stress contour for the validation model: (a) including the curing effect; (b) without curing effect
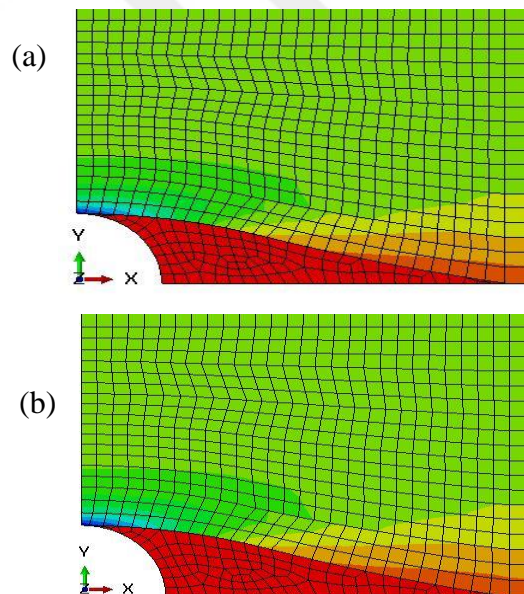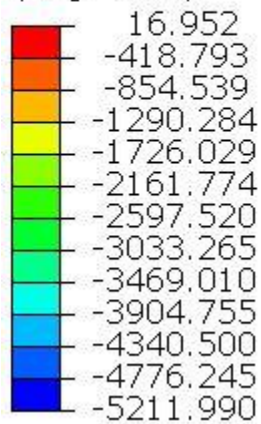
Figure 5.9: Transversal stress contour for the validation model: (a) including the curing effect; (b) without curing effect

5.3 Present Models Results

In this part, various graphical results and stress contours for the present 3D model are obtained. Initially, the stress distribution comparison between the model with real sample dimensions versus the scaled dimensions are presented. After that, several graphical results for the case studies mentioned in Chapter 4 are displayed and discussed.

5.3.1 Scaling Results

In order to thoroughly study the effect of the different vascular sizes in conjunction with diverse stacking sequences, several trial analyses are performed. It will be waste of time doing these models using the true dimensions due to the large number of elements that would be needed around the vascule. For these reasons, a scaled model is made with 1:10 the true length of the tensile test specimen given in ASTM-D 3039. The models are subjected to the same tensile strain of 1%. Figure **5.10** shows the longitudinal stress contours for the true model, while Figure **5.11** displays the longitudinal stress contours for the scaled model. It can be easily observed that the two models have about the same maximum and minimum stresses, and there is an insignificant difference between them. Therefore, the scaled model is used for the rest of the study
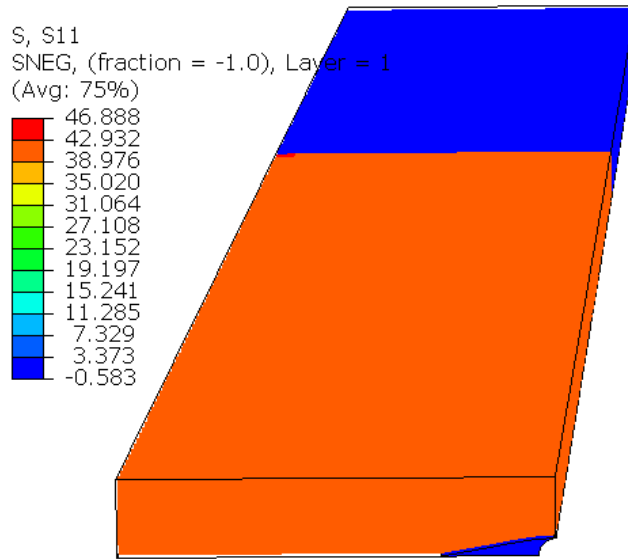
Figure 5.10: Longitudinal stress contour for the middle section of the true dimension model
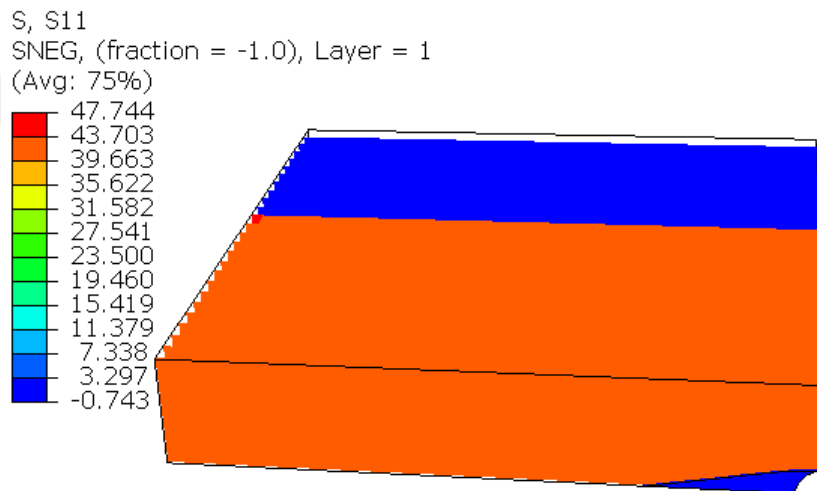
Figure 5.11: Longitudinal stress contour for the middle section of the scaled model

51

5.3.2 Case Study Results

5.3.2.1 Effect of Stacking Configuration

Initially, the effect of stacking configuration for a single vascule diameter is presented. Figures **5.12**, **5.13**, **5.14**, and **5.15** shows the longitudinal and transversal stresses along two paths for various stacking configurations. Here, z-direction is the tensile direction, x-direction is the transverse direction and y is the stacking direction (See Figure **4.12**). The first path above the resin-rich pocket from point B to point A and the second path in the middle of the resin-rich pocket from point C to point A. the *x-axis* are introduced as a normalized distance of these paths as similar to the validation model. The *y-axis* designates the SCF (normalized stress) as a stress component divided by σ_o. All of these plots are for vascular size of 1mm with four different stacking orders ($[0]_{16}$, $[90]_{16}$, $[0/90]_{4s}$, and $[90/0]_{4s}$).
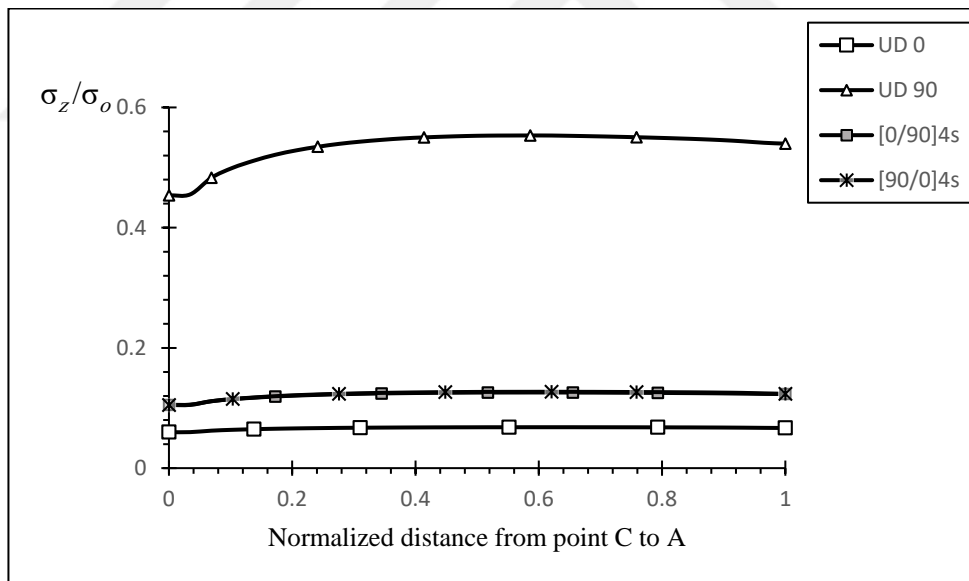
Figure 5.12: Normalized σ_z distribution for 1mm vascule sample with different stacking sequence

According to Figure **5.12** it can be observed that the stress concentration results for the stacking configuration UD 90 has a higher normalized stress and UD 0 has the lowest. This can be explained as follows: The resin-rich pocket carries more longitudinal force when the laminate is UD 90 compared to the other stacking configurations. Thus, the effect of stress concentrations is more effective for this

configuration. Since UD 0 has the highest stiffness, most of the load is carried by the laminate rather than the resin rich region. Thus, the tensile stress concentrations on the resin region are the lowest. As expected, the results of the models with [0/90]$_{4s}$ and [90/0]$_{4s}$ are somewhere between the same results obtained for UD 0 and UD 90 stacking configurations. When compared with each other, the results obtained for [0/90]$_{4s}$ and [90/0]$_{4s}$ are almost the same even though the laminas just above the resin pocket and the dimensions of the resin pocket are different. This is an interesting result as this shows the choice of the lamina stacking order is not effective on the stress distributions near vascular channel.
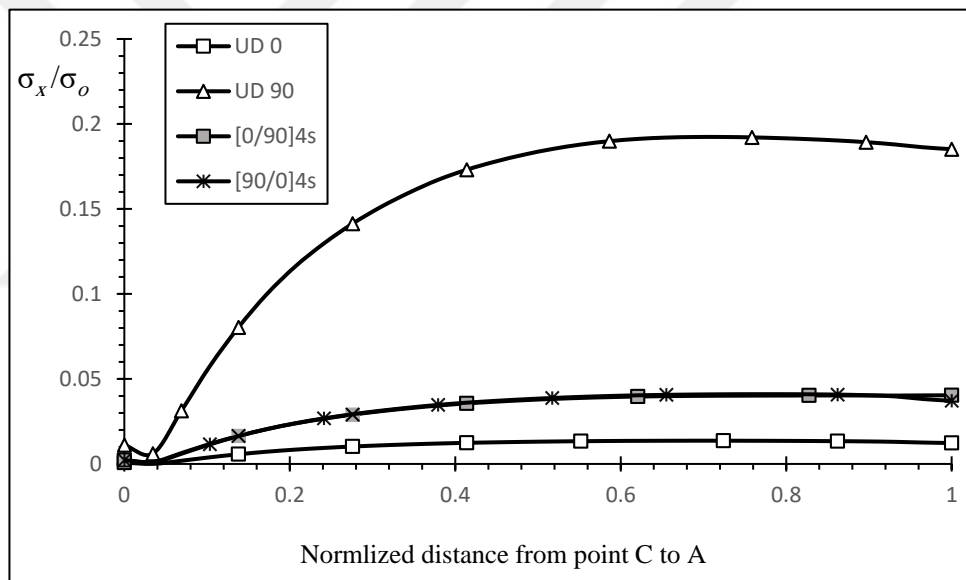
Figure 5.13: Normalized σ_x distribution for 1mm vascule sample with different stacking sequence
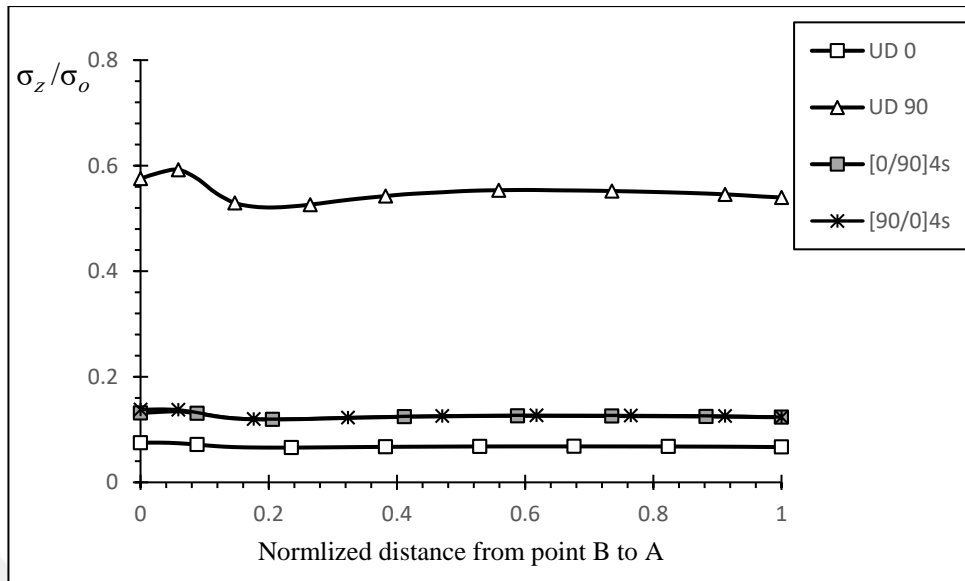
Figure 5.14: Normalized σ$_z$ distribution for 1mm vascule sample with different stacking sequence

Figures **5.13** and **5.14** show the similar trend of Figure **5.12**. The resin-rich pocket gets the higher stress concentrations when the composite laminate is UD 90 and opposite is true for UD 0. The normalized stresses for [0/90]$_{4s}$ and [90/0]$_{4s}$ along the edge from point B to point A also showing no notable differences between these two stacking orders.
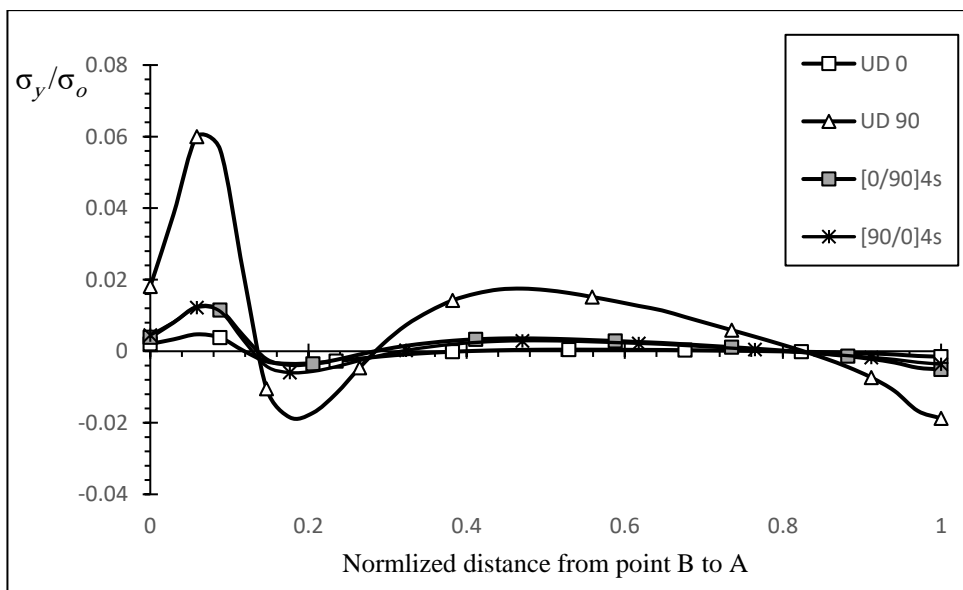
Figure 5.15: Normalized σ$_y$ distribution along the *y-axis* for 1mm vascule sample with different stacking sequence

The most oscillated transversal stress along the edge from point B to the end of the resin-rich pocket at point A are observed for the UD 90 in Figure **5.15**. This behaviour is the result of low resistance of composite laminate to the stress in the thickness direction. While on the other extreme, UD 0 has the least stress differences and concentrations than the other sequences. In between these two stacking orders laminates yet closer to UD 0 is $[0/90]_{4s}$ and $[90/0]_{4s}$.

The stress distribution contours for 1mm diameter of vascular size with ($[0]_{16}$, $[90]_{16}$, $[0/90]_{4s}$, and $[90/0]_{4s}$) are displayed in Figure **5.16**. It is easy to notice that (d) has a higher tensile stress concentration at point B where the laminate above the resin is UD 90. It was also observed that the stresses are more concentrated close to the vascular region in UD 90 model whereas a more homogeneous distribution is observed in UD 0 model. The $[0/90]_{4s}$, and $[90/0]_{4s}$ results lie somewhere between these two extremes. The stress distribution in those models are very close to each other even though they have different resin pocket dimensions.
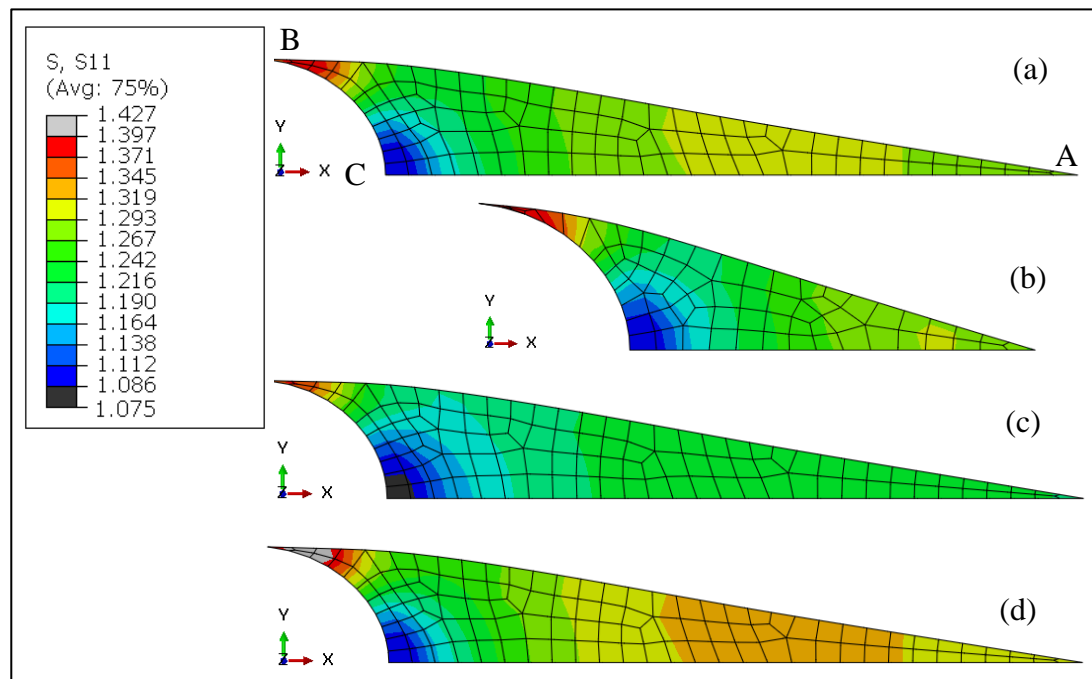
Figure 5.16: Longitudinal stress distribution for different stacking order above the resin-rich pocket: (a) $[0/90]_{4s}$; (b) $[90/0]_{4s}$; (c) $[0]_{16}$; and (d) $[90]_{16}$

The trivial difference between [0/90]$_{4s}$ and [90/0]$_{4s}$ led to a conclusion that the stacking orders [0/90]$_{4s}$ and [90/0]$_{4s}$ have similar effect on the stress distributions. For this reason, there is no need to plot any further graphical results for [90/0]$_{4s}$ stacking order separately.

5.3.2.2   Effect of Vascule Diameter

In order to compare the effect of various vascule diameters, several graphical results are plotted with vascule diameters of 1mm, 0.8mm, 0.6mm, and 0.4mm with the stacking orders [0/90]$_{4s}$, [0]$_{16}$, and [90]$_{16}$. Only normalized longitudinal stress results (σ_z/σ_o) are presented as this stress is the most critical one under tensile loading

Figure **5.17**, Figure **5.18**, and Figure **5.19** illustrate the behaviour of the longitudinal stress in the middle of the resin-rich pocket (i.e. from point C till the end of the pocket at point A). Still, they all show the same tendency along the resin-rich pocket. It can be observed that the stress for 1mm starts lower from the rest and ends above them. This shows that the stresses are more concentrated when the vascule diameter is higher whereas a better distribution of stresses are observed for lower vascule diameters.

Table **8** shows and compares the maximum normalized stresses in longitudinal direction for various vascule diameters. When different stacking conditions are compared with each other, the maximum normalized stress differences between various vascule diameters are higher in UD 0 compared to the other stacking configurations although the values are lower. Thus, it can be concluded that the change in the vascule diameter is more effective for UD 0 lamina than the other stacking configurations
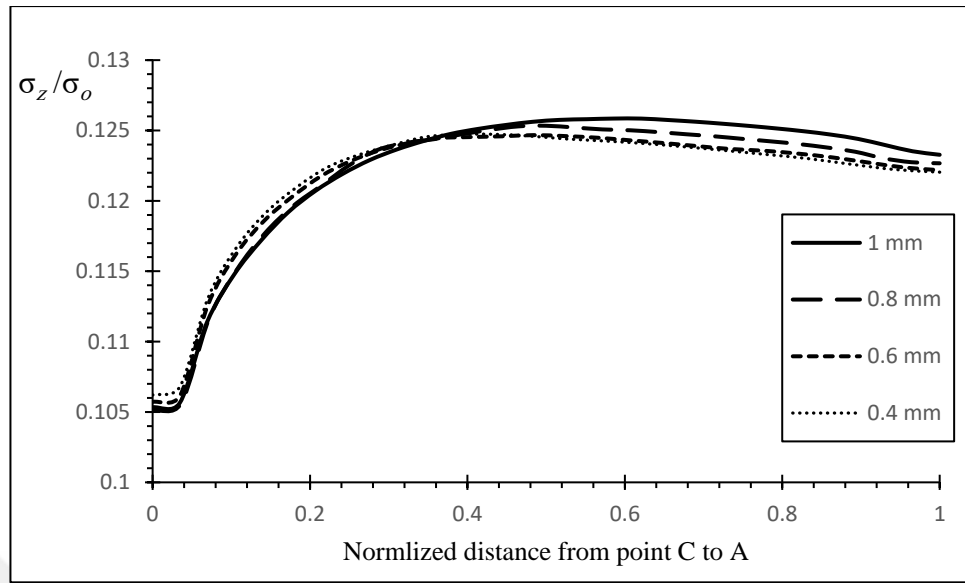
Figure 5.17: Normalized σ_z distribution for different vascular diameters with $[0/90]_{4s}$ stacking sequence
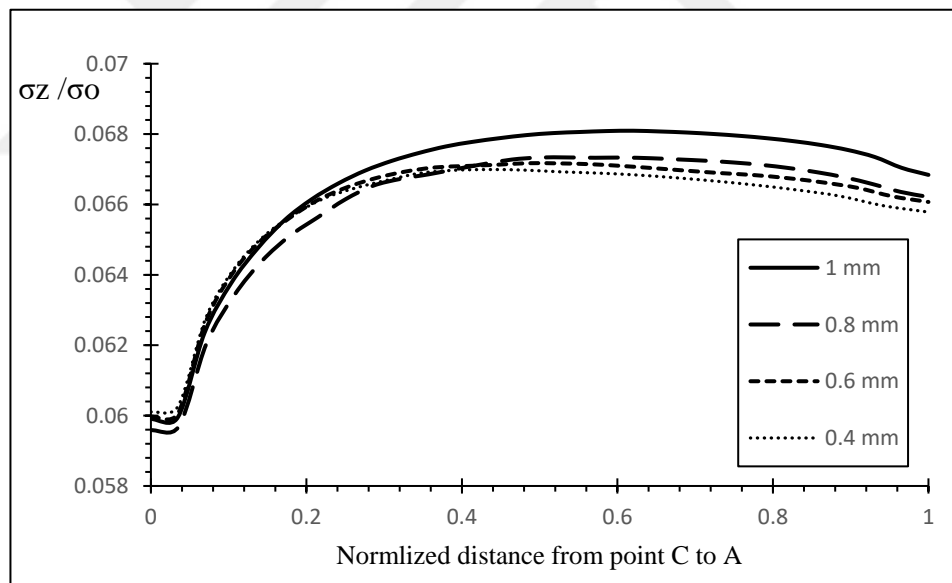
Figure 5.18: Normalized σ_z distribution for different vascular diameter with $[0]_{16}$ stacking sequence

Figure 5.19: Normalized σ_z distribution along the *x-axis* for different vascular diameter with $[90]_{16}$ stacking sequence

Table 8: Maximum normalized σ_z and its relative change for different configurations

	Vascule diameter			
	1 mm	0.8 mm	0.6 mm	0.4 mm
Maximum σ_z/σ_o for UD 0	0.0681	0.06734	0.06717	0.067
Maximum σ_z/σ_o (relative to 1 mm vascule diameter) for UD 0	1	0.9888	0.9863	0.9838
Maximum σ_z/σ_o for UD 90	0.5534	0.5514	0.5498	0.5498
Maximum σ_z/σ_o (relative to 1 mm vascule diameter) for UD 90	1	0.9964	0.9935	0.9935
Maximum σ_z/σ_o for $[0/90]_{4s}$	0.12585	0.12534	0.1247	0.1247
Maximum σ_z/σ_o (relative to 1 mm vascule diameter) for $[0/90]_{4s}$	1	0.996	0.991	0.991

Figure **5.20**, Figure **5.21**, and Figure **5.22** are displaying the normalized longitudinal stress on the edge above the resin-rich pocket (from point B which is located above the vascule till the end of the pocket at point A). These graphs show a sharp inclination of stresses in the region neighbouring the vascule then a state of resilience can be observed as it goes to the end of the pocket. However, in the composite of $[0]_{16}$ laminate the stress recovery is lower than $[0/90]_{4s}$ and $[90]_{16}$. This behavior is due to the higher stiffness of the laminate in that stacking order. The difference between the stresses for various diameters at point B are similar in the stacking orders of $[0/90]_{4s}$ and $[90]_{16}$ whereas a clear distinction between the stresses are observed for $[0]_{16}$. This also shows that changing the vascule diameter is more critical for $[0]_{16}$ stacking configuration.

The stress contours in the resin-rich pocket for $[0/90]_{4s}$ stacking order are depicted in Figure **5.23**. The longitudinal stress near point C is lower compared to the one at point B (top of the vascule). A larger high stress area can be observed in the case of vascule diameter 1 mm compared to the ones with smaller diameters. This clearly reveals the effect of having larger diameter in the stress distributions.
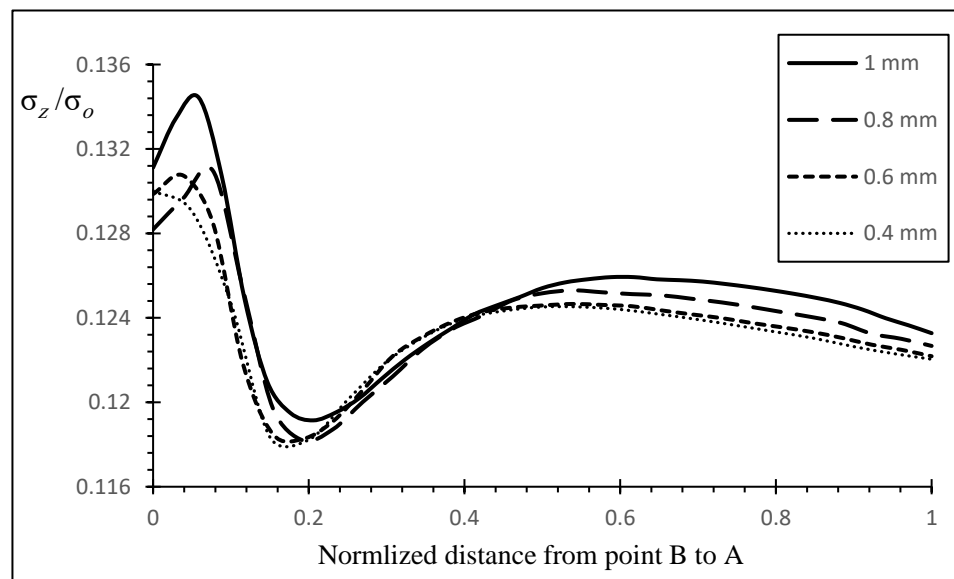
Figure 5.20: Normalized σ_z distribution along the *x-axis* for different vascular diameter with $[0/90]_{4s}$ stacking sequence

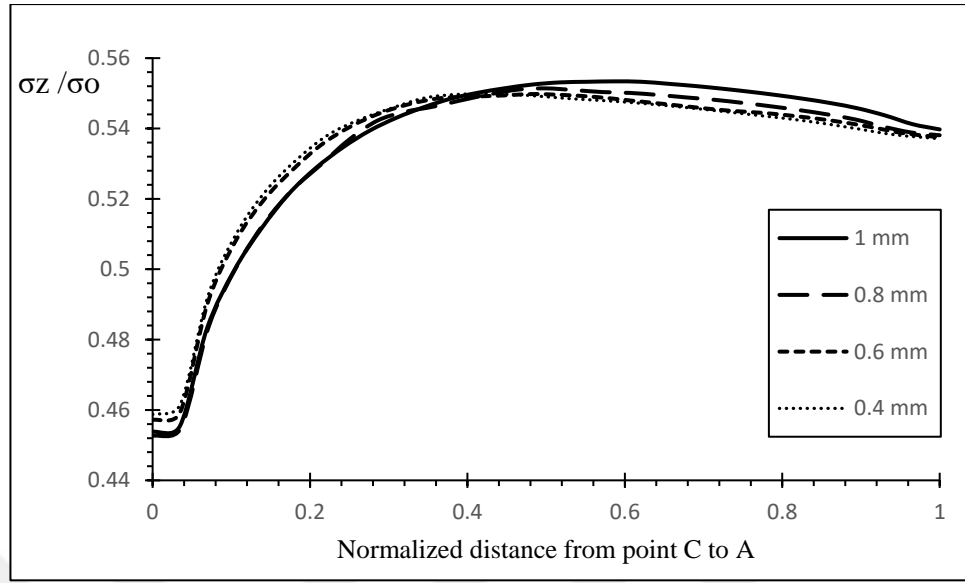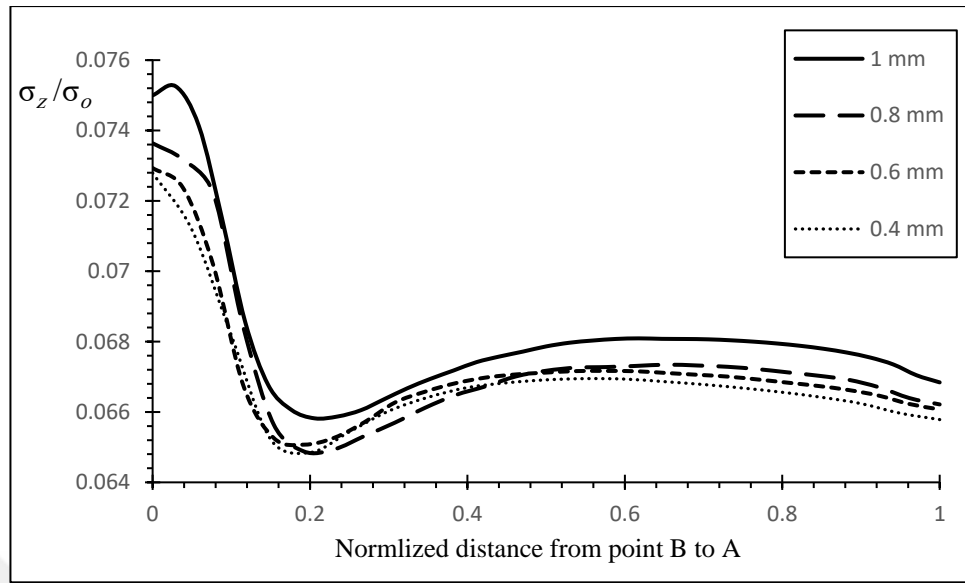**Figure 5.21**: Normalized σ_z distribution along the *x-axis* for different vascular diameter with $[0]_{16}$ stacking sequence
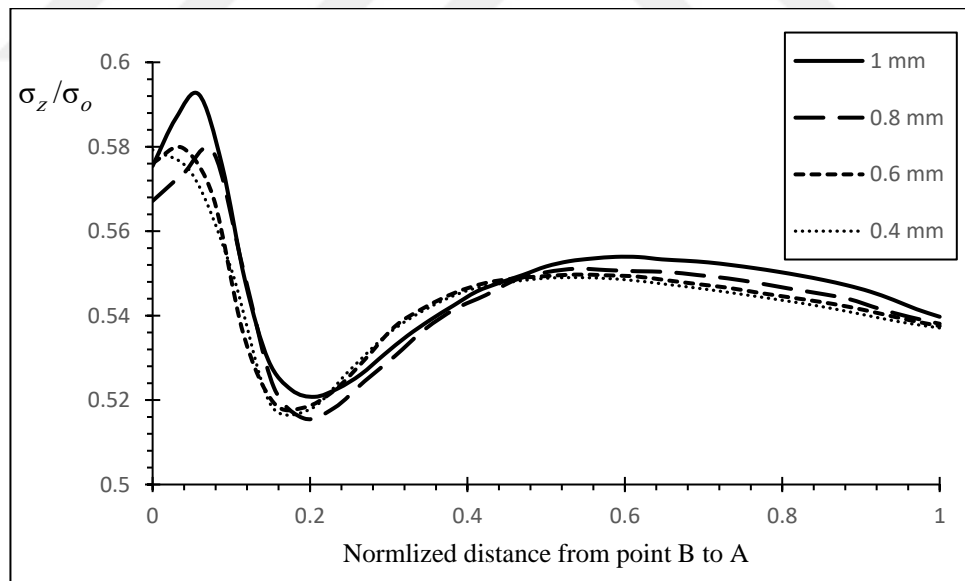
Figure 5.22: Normalized σ_z distribution along the *x-axis* for different vascular diameter with $[90]_{16}$ stacking sequence

60
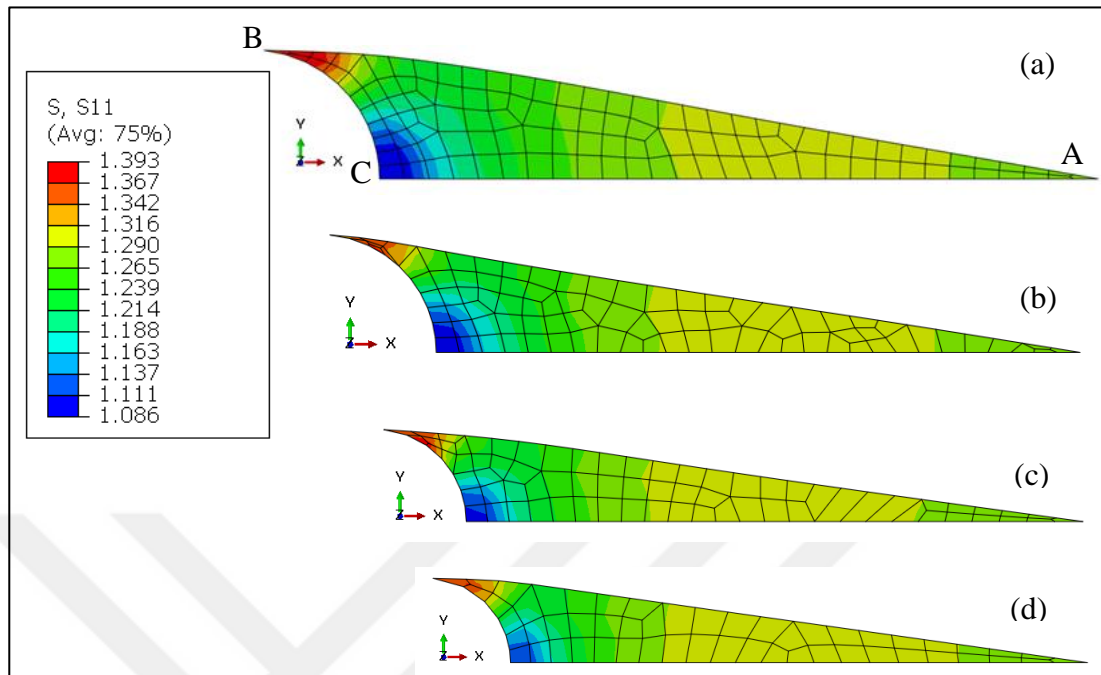
Figure 5.23: Longitudinal stress for [0/90]₄ₛ stacking order: (a) 1 mm vascule diameter; (b) 0.8 mm vascule diameter; (c) 0.6 mm vascule diameter; (d) 0.4 mm vascule diameter

5.3.2.3 Effect of Vascule Shape

The variation of longitudinal stress concentrations for vascules with elliptical shapes are shown in Figure **5.24** along with the results obtained from the vascule diameter of 1mm and 0.8 mm which have almost the same area with the 1st and 2nd ellipse respectively. Both elliptical vascules show a noticeable reduction of the stresses around the resin-rich pocket region compared to their circular counterparts. This reveals the advantage of using elliptical vascule shapes instead of circular ones for lower stress concentrations.

The stress contours for the vascules of 1st elliptical shape and 1mm diameter are shown in Figure **5.25**. Apparently, a reduction of stresses is observed near the vascule when elliptical configuration is used instead of circular one having the same area.
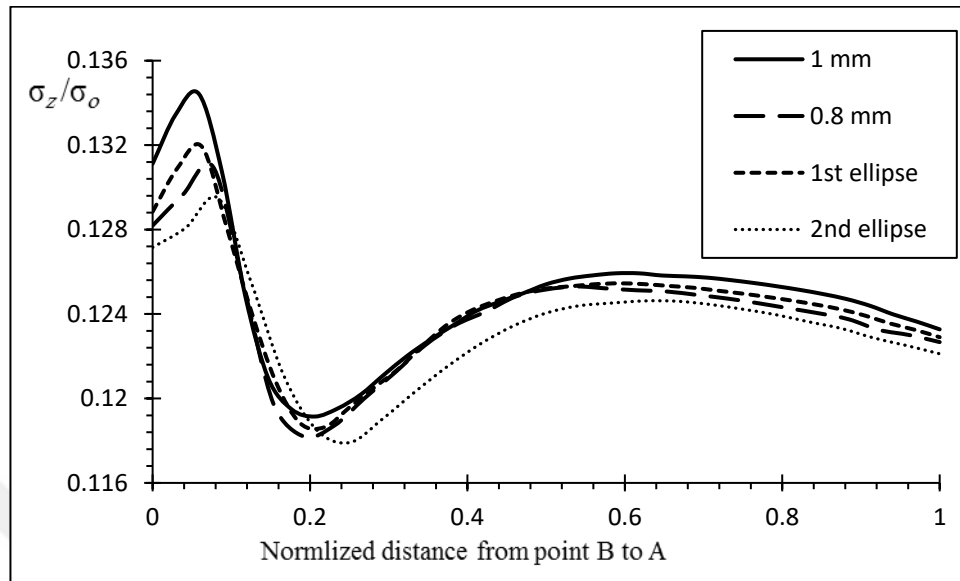
Figure 5.24: Normalized σ_z distribution along the *x-axis* for different vascule shape with [0/90]$_{4s}$ stacking sequence
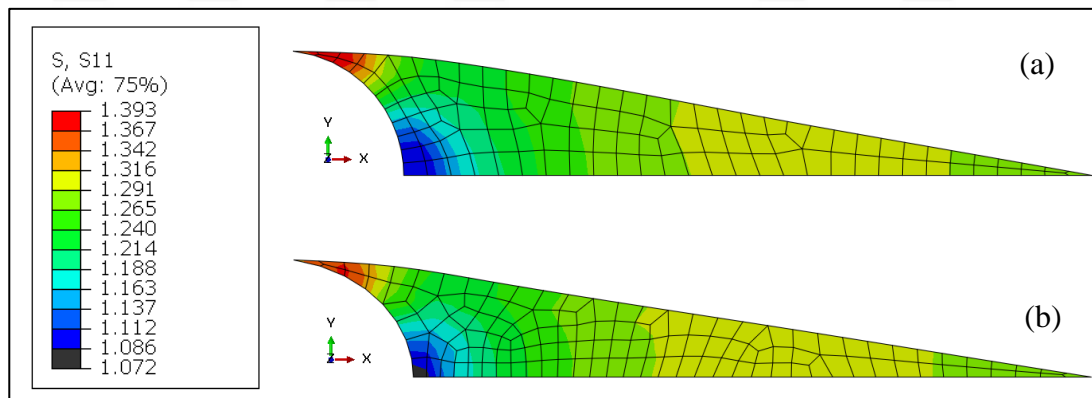
Figure 5.25: Longitudinal stress for [90]$_{16}$ stacking configuration: (a) 1 mm circular vascule; (b) 1st elliptical vascule

5.3.2.4 Other Mechanical Property Results

In the last section, other mechanical properties obtained from all of the case studies are presented in Figure **5.26** and Table **9**. As a constant elongation is introduced to each model, the models with UD 90 give lowest stiffness results whereas the ones with UD 0 give the highest stiffness. The results obtained from [0/90]$_{4s}$ and [90/0]$_{4s}$

stacking configurations give somewhere between those two. The decrease in the vascule diameter results in the increase in Young's modulus. In case of a homogeneous material, when a hole is made in the structure, the Young's modulus cannot change. However, in microvascular channels in composites, such holes generate a larger resin rich zone which increases the percentage of weaker material (i.e. resin) in the cross section. Thus, the Young's modulus decreases. The results for a single layer are very close to each other revealing that the effect of microvascular channels are very low in terms of changing the mechanical behavior for the studied configurations. However, the microvascular channels are modelled for a stacking of 16 plies in this study. If number of plies are decreased and/or number of channels introduced in a single model is increased, the difference between the results can increase drastically.
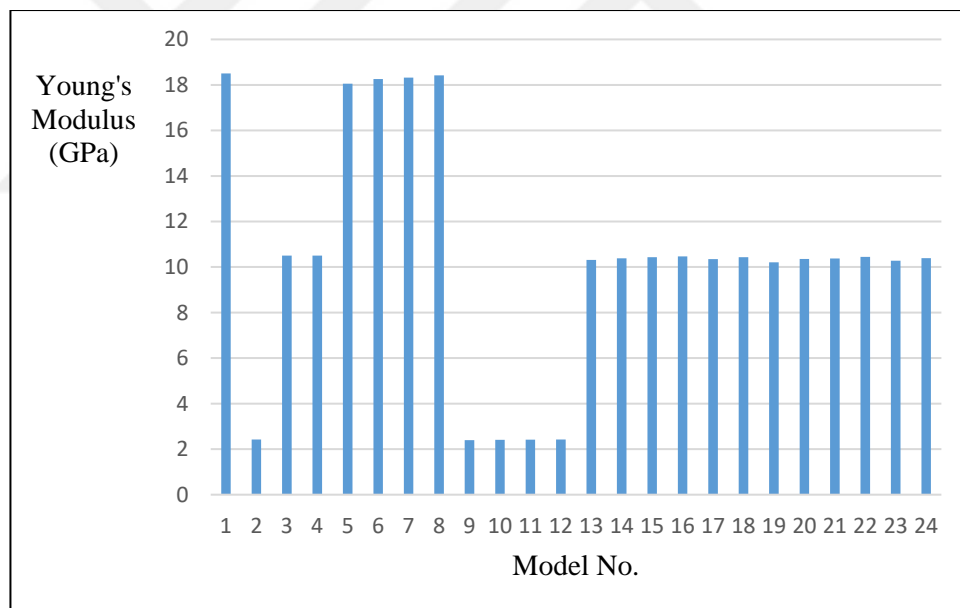
Figure 5.26: Young's modulus for the parametric models

Table 9: Parametric sample models results

No.	Lamination sequence	Vascule diameter (mm)	Reaction Forces (N)	Area (mm^2)	Tensile stress (MPa)	Young modulus (GPa)
1	UD 0	0	520.476	28.125	18.50581	18.506
2	UD 90	0	68.204	28.125	2.425031	2.425
3	[0/90]$_{4s}$	0	295.372	28.125	10.50212	10.502
4	[90/0]$_{4s}$	0	295.354	28.125	10.50148	10.501
5		1	504.23	27.92875	18.05416	18.054
6	UD 0	0.8	511.214	27.9994	18.25803	18.258
7		0.6	513.99	28.05435	18.32122	18.321
8		0.4	517.501	28.0936	18.4206	18.421
9		1	66.906	27.92875	2.395596	2.396
10	UD 90	0.8	67.451	27.9994	2.409016	2.409
11		0.6	67.703	28.05435	2.41328	2.413
12		0.4	67.981	28.0936	2.419804	2.420
13		1	288.031	27.92875	10.31306	10.313
14		0.8	290.77	27.9994	10.38487	10.385
15	[0/90]$_{4s}$	0.6	292.649	28.05435	10.4315	10.432
16		0.4	294.05	28.0936	10.4668	10.467
17		1st ellipse	289.08	27.92877	10.35062	10.351
18		2nd ellipse	292.17	27.9994	10.43487	10.435
19		1	285.08	27.92875	10.2074	10.207
20		0.8	289.89	27.9994	10.35344	10.353
21	[90/0]$_{4s}$	0.6	291.05	28.05435	10.37451	10.375
22		0.4	293.45	28.0936	10.44544	10.445
23		1st ellipse	287.06	27.92877	10.2783	10.278
24		2nd ellipse	290.83	27.9994	10.387	10.387

CHAPTER SIX

CONCLUSION

6.1 Summary

Numerical modelling is an essential tool for the designers in furtherance of fully understand the mechanical behaviour of materials before the final product is manufactured. In this study, a numerical modelling method was developed in order to investigate the stress concentrations in composites with microvascular channels considering various vascule sizes, shapes and stacking sequences. The computational modelling for microvascular channels is achieved by using finite element modeling method. The microvascular channels are modelled parametrically in ABAQUS/Standard finite element solving software. The model geometry is captured directly from a micro-image of a tensile specimen prepared at UTAA labs. The study began with an abridged depiction for the mechanics of composites. Followed by a review of the prior studies on the application, manufacturing, and testing of the microvascular channels. The development of the 3D validation model upon previous 2D model pursued by the present parametric models is presented in chapter four. Then the results for both validation and present models are plotted and discussed by conducting several analyses for various configurations.

6.2 Key Findings and Outcomes

The research performed in this study uncovered many outcomes and key findings which can be summarised as follows;

- A 3D modelling for the microvascular channels embedded in the composite laminate is introduced and verified which more flexible than the models in literature in terms of boundary conditions, loading configurations, stacking sequence and channel direction.

- The stress above and through the middle of the resin-rich pocket preserve its behaviour for various vascular diameters with the same stacking order.

- When the laminate above the pocket is in UD 0, lowest normalized stresses are observed. While in UD 90, normalized stresses are the highest.

- The effect of changing vascule diameters are more effective for UD 0 plies compared to the other stacking configurations.

- The $[0/90]_{4s}$ and $[90/0]_{4s}$ had almost the same attitude under tensile load in all directions. The difference in the resin rich zone dimensions does not affect the results.

- The smaller vascular diameter led to a higher modulus of elasticity. However, the presence of the vascule surprisingly reduces the stiffness of the sample by less than 2% of its stiffness without any vascule. However, this outcome is obtained for a stacking of 16 plies in this study. If number of plies are decreased and/or number of channels introduced in a single model is increase, the difference between the results can increase drastically.

- The models demonstrate that the elliptical vascules show a noticeable reduction of the stresses around the resin-rich pocket region compared to their circular counterparts. For that reason, utilizing a microvascular channel as an elliptical shape rather than circular with the same cross-sectional area reduces the stress concentrations.

6.3   Future Studies

Due to the results and outcomes of the research, following studies are proposed as potential future studies. proposals are presented for the future studies:

1) The effect under different types of loading can be investigated due to model being flexible. For example, the results of applying bending load produce interesting results

2) The effect of two or more channels in the same sample can be investigated. The interaction of channels can affect the stress distribution drastically depending on the distance between them.

3) Various channel orientations and can be analyzed as depending on the service conditions a network of channels may be needed [74].

REFERENCES

[1]   R. F. Gibson, *Principles of Composite Material Mechanics*. McGraw Hill, Inc, 1994.

[2]   A. K. Kaw, *Mechanics of Composite Materials, Second Edition*. CRC Press, 2005.

[3]   P. K. Mallick, *Fiber-Reinforced Composites: Materials, Manufacturing, and Design, Third Edition*. CRC Press, 2007.

[4]   L. Ye, Y. Lu, Z. Su, and G. Meng, "Functionalized composite structures for new generation airframes: a review," *Composites Science and Technology,* vol. 65, no. 9, pp. 1436-1446, 7// 2005.

[5]   S. Rana and R. Fangueiro, "Advanced composites in aerospace engineering," in *Advanced Composite Materials for Aerospace Engineering*: Woodhead Publishing, 2016, pp. 1-15.

[6]   J. Njuguna and K. Pielichowski, "Polymer Nanocomposites for Aerospace Applications: Properties," *Advanced Engineering Materials,* vol. 5, no. 11, pp. 769-778, 2003.

[7]   J. Baur and E. Silverman, "Challenges and Opportunities in Multifunctional Nanocomposite Structures for Aerospace Applications," *MRS Bulletin,* vol. 32, no. 4, pp. 328-334, 2011.

[8]   D. S. S. Enrique J. Garcia , Ludovico Megalini , A. John Hart , Roberto Guzman De Villoria , Brian L. Wardle, "Fabrication and multifunctional properties of high volume fraction aligned carbon nanotube thermoset composites," *Journal of Nano Systems & Technology,* no. October, 2009, 2009.

[9]   N. K. James, D. van den Ende, U. Lafont, S. van der Zwaag, and W. A. Groen, "Piezoelectric and mechanical properties of structured PZT–epoxy composites," *Journal of Materials Research,* vol. 28, no. 4, pp. 635-641, 2013.

[10]   N. K. James, U. Lafont, S. van der Zwaag, and W. A. Groen, "Piezoelectric and mechanical properties of fatigue resistant, self-healing PZT–ionomer composites," *Smart Materials and Structures,* vol. 23, no. 5, p. 055001, 2014.

[11]   K. S. C. Kuang and W. J. Cantwell, "Use of conventional optical fibers and fiber Bragg gratings for damage detection in advanced composite structures: A review," *Applied Mechanics Reviews,* vol. 56, no. 5, pp. 493-513, 2003.

[12]   S. Minakuchi and N. Takeda, "Recent advancement in optical fiber sensing for aerospace composite structures," *Photonic Sensors,* vol. 3, no. 4, pp. 345-354, 2013.

[13]   Q. Meng and J. Hu, "A review of shape memory polymer composites and blends," *Composites Part A: Applied Science and Manufacturing,* vol. 40, no. 11, pp. 1661-1672, 2009.

[14]   J. L. S. Du, *Shape-memory polymers and multifunctional composites*. Boca Raton: Taylor & Francis, 2010.

[15]   L. Yanju, D. Haiyang, L. Liwu, and L. Jinsong, "Shape memory polymers and their composites in aerospace applications: a review," *Smart Materials and Structures,* vol. 23, no. 2, p. 023001, 2014.

[16] A. M. Aragón *et al.*, "Computational design and optimization of a biomimetic self-healing/cooling composite material," vol. 6526, p. 65261G, 2007.

[17] B. D. Kozola, L. A. Shipton, V. K. Natrajan, K. T. Christensen, and S. R. White, "Characterization of Active Cooling and Flow Distribution in Microvascular Polymers," *Journal of Intelligent Material Systems and Structures,* vol. 21, no. 12, pp. 1147-1156, 2010.

[18] R. S. Trask, G. J. Williams, and I. P. Bond, "Bioinspired self-healing of advanced composite structures using hollow glass fibres," *J R Soc Interface,* vol. 4, no. 13, pp. 363-71, Apr 22 2007.

[19] I. Bond, S. White, and N. Sottos, "Introduction: self-healing polymers and composites," *Journal of The Royal Society Interface,* vol. 4, no. 13, pp. 347-348, 2007.

[20] J. P. Youngblood and N. R. Sottos, "Bioinspired Materials for Self-Cleaning and Self-Healing," *MRS Bulletin,* vol. 33, no. 8, pp. 732-741, 2011.

[21] D. Y. Wu, S. Meure, and D. Solomon, "Self-healing polymeric materials: A review of recent developments," *Progress in Polymer Science,* vol. 33, no. 5, pp. 479-522, 2008.

[22] E. B. Murphy and F. Wudl, "The world of smart healable materials," *Progress in Polymer Science,* vol. 35, no. 1-2, pp. 223-251, 2010.

[23] M. Q. Zhang and M. Z. Rong, *Basics of Self-Healing: State of the Art* (Self-Healing Polymers and Polymer Composites). John Wiley & Sons, Inc., 2011.

[24] S. Minakuchi, D. Sun, and N. Takeda, "Hierarchical system for autonomous sensing-healing of delamination in large-scale composite structures," *Smart Materials and Structures,* vol. 23, no. 11, p. 115014, 2014.

[25] T. J. Swait *et al.*, "Smart composite materials for self-sensing and self-healing," *Plastics, Rubber and Composites,* vol. 41, no. 4-5, pp. 215-224, 2013.

[26] J. W. C. Pang and I. P. Bond, "A hollow fibre reinforced polymer composite encompassing self-healing and enhanced damage visibility," *Composites Science and Technology,* vol. 65, no. 11-12, pp. 1791-1799, 2005.

[27] J. W. C. Pang and I. P. Bond, "Self-repair and enhanced damage visibility in a hollow fibre reinforced plastic," in *11th European Conference on Composite Materials, Rhodes, Greece*, vol. Paper B013, 2004.

[28] A. R. Hamilton, N. R. Sottos, and S. R. White, "Local Strain Concentrations in a Microvascular Network," *Experimental Mechanics,* vol. 50, no. 2, pp. 255-263, 2010// 2010.

[29] A. S. Wu *et al.*, "Sensing of damage and healing in three-dimensional braided composites with vascular channels," *Composites Science and Technology,* vol. 72, no. 13, pp. 1618-1626, 8/22/ 2012.

[30] R. S. Trask and I. P. Bond, "Bioinspired engineering study of Plantae vascules for self-healing composite structures," *Journal of The Royal Society Interface,* 10.1098/rsif.2009.0420 vol. 7, no. 47, p. 921, 2010.

[31] C. J. Norris, G. J. Meadway, M. J. O'Sullivan, I. P. Bond, and R. S. Trask, "Self-Healing Fibre Reinforced Composites via a Bioinspired Vasculature," *Advanced Functional Materials,* vol. 21, no. 19, pp. 3624-3633, 2011.

[32] C. J. Norris, I. P. Bond, and R. S. Trask, "The role of embedded bioinspired vasculature on damage formation in self-healing carbon fibre reinforced

composites," *Composites Part A: Applied Science and Manufacturing,* vol. 42, no. 6, pp. 639-648, 6// 2011.

[33]   C. Y. Huang, R. S. Trask, and I. P. Bond, "Characterization and analysis of carbon fibre-reinforced polymer composite laminates with embedded circular vasculature," *Journal of The Royal Society Interface,* 10.1098/rsif.2009.0534 vol. 7, no. 49, p. 1229, 2010.

[34]   C. J. Norris, I. P. Bond, and R. S. Trask, "Interactions between propagating cracks and bioinspired self-healing vascules embedded in glass fibre reinforced composites," *Composites Science and Technology,* vol. 71, no. 6, pp. 847-853, 4/12/ 2011.

[35]   C. J. Norris, I. P. Bond, and R. S. Trask, "Healing of low-velocity impact damage in vascularised composites," *Composites Part A: Applied Science and Manufacturing,* vol. 44, pp. 78-85, 1// 2013.

[36]   J.-C. Hung, D.-H. Chang, and Y. Chuang, "The fabrication of high-aspect-ratio micro-flow channels on metallic bipolar plates using die-sinking micro-electrical discharge machining," *Journal of Power Sources,* vol. 198, pp. 158-163, 1/15/ 2012.

[37]   A. Kousourakis, A. P. Mouritz, and M. K. Bannister, "Interlaminar properties of polymer laminates containing internal sensor cavities," *Composite Structures,* vol. 75, no. 1–4, pp. 610-618, 9// 2006.

[38]   C. M. Dry and N. R. Sottos, "Passive smart self-repair in polymer matrix composite materials," 1993, vol. 1916, pp. 438-444.

[39]   J. G. Hemrick, E. Lara-Curzio, E. R. Loveland, K. W. Sharp, and R. Schartow, "Woven graphite fiber structures for use in ultra-light weight heat exchangers," *Carbon,* vol. 49, no. 14, pp. 4820-4829, 11// 2011.

[40]   C. Dry, "Procedures developed for self-repair of polymer matrix composite materials," *Composite Structures,* vol. 35, no. 3, pp. 263-269, 1996/07/01 1996.

[41]   C. M. Dry, "Self-repairing, reinforced matrix materials," ed: Google Patents, 2003.

[42]   C. M. Dry, "Self-repairing, reinforced matrix materials," ed: Google Patents, 2001.

[43]   M. Motuku, U. K. Vaidya, and G. M. Janowski, "Parametric studies on self-repairing approaches for resin infused composites subjected to low velocity impact," *Smart Materials and Structures,* vol. 8, no. 5, p. 623, 1999.

[44]   D. Roach, "Real time crack detection using mountable comparative vacuum monitoring sensors," *Smart Structures and Systems,* vol. 5, no. 4, pp. 317–28, 2009.

[45]   B. D, "Comparative Vacuum Monitoring: a New Method of In-Situ Real-Time Crack Detection and Monitoring," *Structural Monitoring Systems Ltd.,* no. 2004, 2004.

[46]   B. IP, "Self-repairing hollow fibre composites," *Reinforced Plastics,* vol. 48, no. 8, p. 16, 9// 2004.

[47]   M. J. Hucker and I. P. Bond, "Optimisation of hollow glass fibres and their composites," in *ICCM-12: 12th International Conference on Composite Materials, Paris June 1999*, vol. Paper 660: Woodhead Publishing Ltd, 1999.

[48] I. Bond, M. Hucker, S. Bleay, and S. Haq, "Optimising the Performance of Hollow Glass Fibre/Epoxy Composites Under Compressive Loading," in *43rd AIAA/ASME/ASCE/AHS/ASC Structures, Structural Dynamics, and Materials Conference*(Structures, Structural Dynamics, and Materials and Co-located Conferences: American Institute of Aeronautics and Astronautics, 2002.

[49] M. J. Hucker, I. P. Bond, S. Haq, S. Bleay, and A. Foreman, "Influence of manufacturing parameters on the tensile strengths of hollow and solid glass fibres," *Journal of Materials Science,* vol. 37, no. 2, pp. 309-315, 2002// 2002.

[50] M. Hucker, I. Bond, S. Bleay, and S. Haq, "Investigation into the behaviour of hollow glass fibre bundles under compressive loading," *Composites Part A: Applied Science and Manufacturing,* vol. 34, no. 11, pp. 1045-1052, 11// 2003.

[51] A. P. Esser-Kahn *et al.*, "Three-Dimensional Microvascular Fiber-Reinforced Composites," *Advanced Materials,* vol. 23, no. 32, pp. 3654-3658, 2011.

[52] S. Soghrati, P. R. Thakre, S. R. White, N. R. Sottos, and P. H. Geubelle, "Computational modeling and design of actively-cooled microvascular materials," *International Journal of Heat and Mass Transfer,* vol. 55, no. 19–20, pp. 5309-5321, 9// 2012.

[53] S. Soghrati *et al.*, "Computational analysis of actively-cooled 3D woven microvascular composites using a stabilized interface-enriched generalized finite element method," *International Journal of Heat and Mass Transfer,* vol. 65, pp. 153-164, 10// 2013.

[54] S. Soghrati, A. M. Aragón, and P. H. Geubelle, "Design of actively-cooled microvascular materials: a genetic algorithm inspired network optimization," *Structural and Multidisciplinary Optimization,* vol. 49, no. 4, pp. 643-655, 2014// 2014.

[55] H. R. Williams, R. S. Trask, and I. P. Bond, "Self-healing composite sandwich structures," *Smart Materials and Structures,* vol. 16, no. 4, p. 1198, 2007.

[56] T. Dixit and I. Ghosh, "Review of micro- and mini-channel heat sinks and heat exchangers for single phase fluids," *Renewable and Sustainable Energy Reviews,* vol. 41, pp. 1298-1311, 1// 2015.

[57] E. Bremus *et al.*, "Laserprocessing for manufacturing microfluidic devices," in *Microreaction Technology: Industrial Prospects: IMRET 3: Proceedings of the Third International Conference on Microreaction Technology*, W. Ehrfeld, Ed. Berlin, Heidelberg: Springer Berlin Heidelberg, 2000, pp. 80-89.

[58] M. S. F. Lima, J. M. S. Sakamoto, J. G. A. Simoes, and R. Riva, "Laser Processing of Carbon Fiber Reinforced Polymer Composite for Optical Fiber Guidelines," *Physics Procedia,* vol. 41, pp. 572-580, 2013/01/01 2013.

[59] J.-H. Huang *et al.*, "Rapid Fabrication of Bio-inspired 3D Microfluidic Vascular Networks," *Advanced Materials,* vol. 21, no. 35, pp. 3567-3571, 2009.

[60] J. A. Lewis, "Direct Ink Writing of 3D Functional Materials," *Advanced Functional Materials,* vol. 16, no. 17, pp. 2193-2204, 2006.

[61] D. Therriault, R. F. Shepherd, S. R. White, and J. A. Lewis, "Fugitive Inks for Direct-Write Assembly of Three-Dimensional Microvascular Networks," *Advanced Materials,* vol. 17, no. 4, pp. 395-399, 2005.

[62]   D. Therriault, S. R. White, and J. A. Lewis, "Chaotic mixing in three-dimensional microvascular networks fabricated by direct-write assembly," *Nat Mater,* 10.1038/nmat863 vol. 2, no. 4, pp. 265-271, 04//print 2003.

[63]   D. Therriault, "Directed assembly of three-dimensional microvascular networks," Ph.D., Aerospace Engineering, University of Illinois at Urbana-Champaign, 2003.

[64]   A. Kousourakis, M. K. Bannister, and A. P. Mouritz, "Tensile and compressive properties of polymer laminates containing internal sensor cavities," *Composites Part A: Applied Science and Manufacturing,* vol. 39, no. 9, pp. 1394-1403, 9// 2008.

[65]   A. M. Coppola, P. R. Thakre, N. R. Sottos, and S. R. White, "Tensile properties and damage evolution in vascular 3D woven glass/epoxy composites," *Composites Part A: Applied Science and Manufacturing,* vol. 59, pp. 9-17, 2014.

[66]   J. F. Patrick *et al.*, "Continuous Self-Healing Life Cycle in Vascularized Structural Composites," *Advanced Materials,* vol. 26, no. 25, pp. 4302-4308, 2014.

[67]   E. J. Barbero, *Finite Element Analysis of Composite Materials using AbaqusTM.* CRC Press, 2013.

[68]   A. T. T. Nguyen and A. C. Orifici, "Structural assessment of microvascular self-healing laminates using progressive damage finite element analysis," *Composites Part A: Applied Science and Manufacturing,* vol. 43, no. 11, pp. 1886-1894, 2012.

[69]   D. J. Hartl, G. J. Frank, and J. W. Baur, "Effects of microchannels on the mechanical performance of multifunctional composite laminates with unidirectional laminae," *Composite Structures,* vol. 143, pp. 242-254, 2016.

[70]   E. J. Barbero, *Introduction to Composite Materials Design, Second Edition.* Taylor & Francis, 2010.

[71]   H. Corporation, "Araldite LY 564/ Aradur 2954," ed, 2011.

[72]   ABAQUS, "Analysis user's manual," ed. Woodlands Hills, CA: Dassault Systèmes of America Corp., 2016.

[73]   K. Shivakumar, "Failure Mechanics of a Composite Laminate Embedded with a Fiber Optic Sensor," *Journal of Composite Materials,* vol. 39, no. 9, pp. 777-798, 2005.

[74]   J. F. Patrick *et al.*, "Robust Sacrificial Polymer Templates for 3D Interconnected Microvasculature in Fiber-reinforced Composites," *Composites Part A: Applied Science and Manufacturing*.